NASA
CR
3294
c.1

NASA Contractor Report 3294

LOAN COPY: RET
AFWL TECHNICA
KIRTLAND AFB
0062077
TECH LIBRARY KAFB, NM

A Parametric Study of Aliasing Error for a Narrow Field of View Scanning Radiometer

Nesim Halyo and Steven T. Stallman

CONTRACT NAS1-15628
AUGUST 1980

NASA

TECH LIBRARY KAFB, NM

0062077

NASA Contractor Report 3294

A Parametric Study of Aliasing Error for a Narrow Field of View Scanning Radiometer

Nesim Halyo and Steven T. Stallman
Information & Control Systems, Incorporated
Hampton, Virginia

Prepared for
Langley Research Center
under Contract NAS1-15628

National Aeronautics
and Space Administration

Scientific and Technical
Information Branch

1980

TABLE OF CONTENTS

		page
I.	Introduction	1
II.	NFOV Scanner Model Development	6
	A. Aliasing Error Model	16
	B. Information Density	29
III.	Results	37
IV.	Conclusions	40
V.	Appendix A	43
	References	63

LIST OF FIGURES

		page
Figure 1	Satellite, Orbit and Top of the Atmosphere Geometry	65
Figure 2	Block Diagram of NFOV Scanner	66
Figure 3	Frequency Response of Detectors	67
Figure 4	Frequency Response of Electrical Filter	68
Figure 5	Wiener Spectra of Sampled Signals	69
Figure 6	Parametric Aliasing Error Curves	70
Figure 7	Parametric Aliasing Error Curves of Smoothed Signals	71
Figure 7	Continued	72
Figure 7	Concluded	73
Figure 8	Circular Aperture with Continuous Scan	74
Figure 9	Aliasing Error Versus μ_r/γ for Smoothed Signals	75
Figure 10	Information Density Transmitted Through Radiometer in Unsmoothed Reconstruction	76

I. INTRODUCTION

The output signal of a radiometer can be expressed in terms of the distribution of incident spectral radiance, the instrument parameters and relative geometry between the source of the radiation and the instrument. The general formulation of this relation is commonly referred to as measurement equation [1]. The application of this measurement equation to the solution of practical measurement problems usually requires some simplifications to obtain a tractable computational model of the measurement process. The primary objectives of this study are: (1) to derive (simplified) formulations of the measurement equation suitable for evaluating effects of the spatial (or angular) response of narrow field-of-view (NFOV) scanning radiometers; and (2) to evaluate effects of the measurement process that are inherent in the reconstruction of a continuous radiance field from discrete radiometric measurements.

In particular, it is shown that appropriate approximations to the measurement equation lead to a convolution integral of the spatial distribution of the spectral radiance and of the radiometer response, and that the accuracy of continuous reconstructions of radiance fields from discrete radiometric measurements is subject to degradation due to blurring and aliasing. It is proved (in the Appendix) that the aliasing errors that are generated if spatial details have been undersampled, can be treated as statistically

independent noise if the radiance field is a (real) Gaussian process. Degradations due to aliasing and blurring are evaluated for a random radiance field with a Wiener spectrum that is representative of a wide range of scenes, and for spatial responses that are typical of televisions and radiometers. In addition, this study also evaluates the information capacity representative of these spatial responses.

This study is part of an undertaking to develop comprehensive analytical and computational measurement models for the Earth Radiation Budget Experiment (ERBE). The results obtained in this study have been used in the ERBE NFOV design and performance trade-off studies.

The measurement of the Earth's radiation balance to refine previous estimates has attracted continuing attention over the last two decades. These efforts, which included experiments on Explorer VII and the Nimbus satellites, have led to the Earth Radiation Budget Experiment sponsored by the National Aeronautics and Space Administration (NASA). The ERBE instruments include wide and medium field-of-view (WFOV and MFOV) radiometers, as well as narrow field-of-view (NFOV) scanners. While the wide field-of-view instruments are useful in obtaining global averages, the narrow field-of-view instrument provides local measurements of radiation, which are useful in the accurate determination of spatial (zonal and regional) variations of the radiant exitance at the top of the atmosphere, and can be used in the estimation of the directional

models of the radiance field. To be useful, an accuracy of 1% for the global mean albedo and radiant exitance ($\bar{a}$ and $\bar{M}_e$, resp.), and an accuracy of ±10 W/m^2 for zonal and regional variations in the short wave (reflected) and long wave (emitted) radiant exitance are generally required for climate monitoring, with more stringent accuracies required for climate theory applications. Thus, it is necessary to determine the accuracy of the measurements and investigate the trade-offs involved between the design parameters and the errors introduced in the measurements of the radiant exitance at the top of the atmosphere.

This work considers the analysis of aliasing error and blurring (or the loss of spatial resolution) introduced into a reconstruction of the radiant exitance when the NFOV scanner output is undersampled. Through mathematical modeling and quantitative analysis, it describes the trade-offs between design parameters such as the sampling interval, detector aperture shape, continuous-scan versus step-scan, etc., and the amount of aliasing error and blurring introduced into a reconstruction of the radiant exitance from the sampled digital radiometer output. The effects of smoothing the estimates, and of varying levels of high spatial frequency content in the radiant exitance at the top of the atmosphere are also considered. To obtain results useful in a more general context, when possible, normalized parameters were used. The degradation of image quality obtained with line-scan devices such as optical-mechanical scanners and television cameras has received considerable attention [2] -

[10]. In these investigations, the emphasis has been placed mainly on the detection, recognition and reproduction of specific detail and objects. The work presented here considers a detailed parametric study of the expected magnitude of aliasing errors contained in the reconstruction of random radiance fluctuations typical of natural scenes, which has been considered only in illustrative examples [7], [11] in the literature.

The block diagram in Fig. 2 shows the main components of the NFOV scanner considered. The radiant exitance M(x,y) at the top of the atmosphere passes through a lens and heats the detector, thus altering its temperature. The change in the temperature is sensed and converted to an electrical signal which is amplified and passed through an electrical filter to reduce the noise due to the detector and aliasing error, before being sampled, digitized and transmitted to earth by telemetry. The sampled signal is then reconstructed to obtain a continuous signal. In most cases, due to limitations in the telemetry transmission rate and the frequency content of the signals, the reconstructed signal differs from the original one; this is referred to as insufficient sampling. The error in the reconstructed signal is called aliasing noise or error. In general, the smaller the sampling interval, the less the aliasing error introduced. However, as can be seen from the results (see section III) the choice of design parameters such as the shape of the detector field of view, the electrical filter, the use of a stepping or a continuous scan system, etc., is of

considerable importance in reducing the aliasing error.

In section II, the relative geometry of the orbit, the top of the atmosphere and scanning pattern (see Fig. 1) are used to show that the output of the detector can be modeled or approximated by passing the radiant exitance through a space-invariant system. Section IIA describes analytical models of the aliasing error and its dependence on the system parameters. Section IIB considers the information density transmitted through the system as a design criterion. Section III describes the results of the parametric study to show the trade-offs involved quantitatively.

II. NFOV SCANNER MODEL DEVELOPMENT

Consider a satellite on a circular orbit about the earth, with radius r + h, where r is the radius of the sphere representing the top of the atmosphere, and h is the altitude of the satellite from the top of the atmosphere, as shown in Fig. 1. The subsatellite points of the orbit form a great circle on the top of the atmosphere. Considering this circle as the equator, a coordinate system with components of longitude (ϕ) and colatitude (θ) can be defined, to represent the points at the top of the atmosphere. Thus, the equator and constant colatitude curves represent the along-track direction, while the constant longitude curves represent the scan direction.

Suppose that, at time t, the subsatellite point has longitude ϕ_1, and that the scan point (the intersection of the optical axis and the top of the atmosphere) has colatitude θ_1, then the detector output, $m(\theta_1, \phi_1)$, due to radiation from the top of the atmosphere can be modeled as (e.g., see [1], Chapter 9)

$$m(\theta_1, \phi_1) = A \iint_{A_1'} \int_0^\infty L_\lambda(\theta, \phi, \theta', \phi') S_\lambda(\chi, \psi) \frac{\cos\theta' \cos\chi}{\rho^2} d\lambda dA' \quad (1)$$

where A is the area of the detector, $L_\lambda(\theta, \phi, \theta', \phi')$ is the spectral radiance at the top of the atmosphere at the point (θ, ϕ) in the direction (θ', ϕ'), $S_\lambda(\chi, \psi)$ is the sensor response for radiation arriving from the direction (χ, ψ) of wavelength λ, ρ is

the distance between the point (θ, ϕ) and the detector, and A_1' is the "footprint" at the top of the atmosphere for the scan point (θ_1, ϕ_1). This is based on assumptions that the instrument is operating in a stable and linear region of its operating range, that the effects of radiation arriving from other sources have been accounted for by ground and in-flight calibration procedures, that the sensor time constants are small compared to variations in the spectral radiance, and that the linear dimensions of the detector surface are much smaller than the distance ρ.

For a narrow field of view sensor, Eq. 1 can be approximated by a convolution as will be shown in the following; this allows the use of Fourier theory in the analysis of the measurement process of the NFOV scanner. The scan point with longitude ϕ_1, colatitude θ_1, and radius r can be represented by a three component vector, z_2, in the rectangular coordinate system shown in Fig. 1, as

$$z_2 = r \begin{bmatrix} \sin\theta_1 \cos\phi_1 \\ \sin\theta_1 \sin\phi_1 \\ \cos\theta_1 \end{bmatrix}. \tag{2}$$

The position of the detector, say z_1, can be expressed as

$$z_1 = (r + h) \begin{bmatrix} \cos\phi_1 \\ \sin\phi_1 \\ 0 \end{bmatrix}. \tag{3}$$

Now let z be a point in the footprint A_1' about the scan point

(θ_1, ϕ_1); let $(\theta_1 - \alpha, \phi_1 - \beta)$ be the colatitude and longitude of z, so that

$$z = r\begin{bmatrix} \sin(\theta_1 - \alpha)\ \cos(\phi_1 - \beta) \\ \sin(\theta_1 - \alpha)\ \sin(\phi_1 - \beta) \\ \cos(\theta_1 - \alpha) \end{bmatrix}. \tag{4}$$

For a narrow field of view instrument, the footprint consists of a small area about the scan point, so that the values of α and β are small. Thus, using small angle approximations,

$$z \simeq r\begin{bmatrix} (\sin\theta_1 - \alpha\ \cos\theta_1)(\cos\phi_1 + \beta\ \sin\phi_1) \\ (\sin\theta_1 - \alpha\ \cos\theta_1)(\sin\phi_1 - \beta\ \cos\phi_1) \\ \cos\theta_1 + \alpha\ \sin\theta_1 \end{bmatrix}. \tag{5}$$

Neglecting the second order terms in (5),

$$z \simeq z_2 - (r\alpha\ u_\theta + r\beta\ \sin\theta_1\ u_\phi), \tag{6}$$

$$u_\theta = \begin{bmatrix} \cos\theta_1\ \cos\phi_1 \\ \cos\theta_1\ \sin\phi_1 \\ -\ \sin\theta_1 \end{bmatrix}, \quad u_\phi = \begin{bmatrix} -\ \sin\phi_1 \\ \cos\phi_1 \\ 0 \end{bmatrix}. \tag{7}$$

It should be noted that u_θ and u_ϕ are orthogonal unit vectors which lie in the plane tangent at the scan point, z_2. Thus, from (6) it is seen that the points in A_1' lie (approximately) on the tangent plane. To illustrate the approach, consider a circular field of view of δ radians, then

$$A_1' = \{(\theta_1-\alpha,\ \phi_1-\beta) \mid 0 \le \chi \le \delta\} = \{(\theta_1-\alpha,\ \phi_1-\beta) \mid 0 \le \sin\chi \le \sin\delta\} \quad (8)$$

For a given scan point, the angle χ is a function of α and β; thus, the constraint on χ in (8) imposes a constraint on α and β, which defines the footprint A_1' more explicitly. To determine the latter constraint, first note that χ is the angle subtended by the optical axis and the line connecting the detector to an arbitrary point in the footprint; i.e., χ is the angle between the vectors $z_2 - z_1$ and $z - z_1$. Hence,

$$\sin\chi = \frac{\|(z_2-z_1) \times (z-z_1)\|}{\|z_2-z_1\| \ \|z-z_1\|}, \quad (9)$$

where $\| \ \|$ denotes Euclidian vector norm, and x denotes the vector product (cross product). Noting that

$$z-z_1 = (z-z_2) + (z_2-z_1)\ ,\ (z_2-z_1) \times (z_2-z_1) = 0 \quad (10)$$

(9) can be expressed as

$$\sin\chi = \frac{1}{\rho\ \rho_2}\ \|(z_2-z_1) \times (z-z_2)\|\ , \quad (11)$$

where

$$\rho = \|z-z_1\|\ ,\quad \rho_2 = \|z_2-z_1\|\ . \quad (12)$$

Using the definition of the vector product,

$$\sin\chi = \frac{1}{\rho\ \rho_2}\left[\rho_2^2\|z-z_2\|^2 - |(z_2-z_1)^T(z-z_2)|^2\right]^{\frac{1}{2}} \quad (13)$$

where the superscript "T" denotes the transpose. From (6), we

obtain

$$\|z-z_2\| \simeq r^2 \|\alpha u_\theta + \beta \sin\theta_1 u_\phi\|^2 \tag{14}$$

$$= r^2 (\alpha^2 + \beta^2 \sin^2\theta_1). \tag{15}$$

Manipulating (2) and (3),

$$\rho_2^2 = \|z_2-z_1\|^2 = r^2 + (r+h)^2 - 2r(r+h) \sin\theta_1. \tag{16}$$

By direct computation, it can be found that

$$(z_2-z_1)^T u_\phi = 0 \tag{17}$$

$$(z_2-z_1)^T u_\theta = -(r+h) \cos\theta_1 \tag{18}$$

$$(z_2-z_1)^T (z-z_2) = -r(z_2-z_1)^T(\alpha u_\theta + \beta \sin\theta_1 u_\phi) \tag{19}$$

$$= - r\alpha(z_2-z_1)^T u_\theta = r(r+h)\alpha \cos\theta_1. \tag{20}$$

Substituting (15) and (20) into (13), and collecting terms,

$$\sin \chi \simeq \frac{r}{\rho \ \rho_2} \left[(\rho_2^2-(r+h)^2 \cos^2\theta_1) \alpha^2 + \rho_2^2 \sin^2\theta_1 \beta^2\right]^{\frac{1}{2}} \tag{21}$$

$$= \frac{r}{\rho \ \rho_2} \left[(r-(r+h) \sin\theta_1)^2 \alpha^2 + \rho_2^2 \sin^2\theta_1 \beta^2\right]^{\frac{1}{2}} \tag{22}$$

where (16) has been used to obtain (22). A further simplification can be obtained by noting that the angle, θ_1', subtended by z_1-z_2 and the normal to the tangent plane at (θ_1, ϕ_1), satisfies

$$\cos\theta_1' = \frac{z_2^T (z_1 - z_2)}{\|z_2\| \; \|z_1 - z_2\|} = \frac{1}{r\,\rho_2} \; (z_2^T \cdot z_1 - r^2) \tag{23}$$

$$= \frac{1}{\rho_2} \left((r+h) \sin\theta_1 - r\right). \tag{24}$$

Substituting (24) into (22), and simplifying

$$\sin\chi \approx \frac{r}{\rho} \left[\cos^2\theta_1' \; \alpha^2 + \sin^2\theta_1 \; \beta^2 \right]^{\frac{1}{2}}. \tag{25}$$

Since the footprint, A_1', corresponds to a small area about the scan point, or alternately since α and β are small for points in A_1', the distance ρ can be approximated by ρ_2. Thus, the footprint can be described by

$$\{(\theta_1 - \alpha,\ \phi_1 - \beta) \,\big|\, \cos^2\theta_1' \; \alpha^2 + \sin^2\theta_1 \; \beta^2 < \frac{\rho_2^2}{r^2} \; \delta^2\} \tag{26}$$

Thus, for a narrow circular field of view, the footprint corresponds to a nearly elliptical surface on top of the atmosphere. At nadir, the footprint becomes circular as a limiting case, since $\theta_1 = \pi/2$ and $\theta_1' = 0$.

It is sometimes more convenient to use distance related variables than latitude and longitude. Thus, consider the following change of variables

$$x = r\phi,\ y = r\theta,\ x' = r\beta,\ y' = r\alpha. \tag{27}$$

In terms of these variables, (1) can be rewritten as

$$m(x_1,y_1) = A \iint_{A_1'} \int_0^\infty L_\lambda(x, y, \theta', \phi')S_\lambda(\chi, \psi) \frac{\cos\theta' \cos\chi}{\rho^2} d\lambda dA'. \quad (28)$$

Now let

$$x = x_1 - x', \; y = y_1 - y'; \quad (29)$$

Then dA' is given by

$$dA' = r^2 \sin\theta \, d\theta \, d\phi = \sin\theta \quad dx'dy'. \quad (30)$$

Define the indicator function of A_1' as

$$I_1(x',y') = \begin{cases} 1, & \sin^2\theta_1 \, x'^2 + \cos^2\theta_1' \quad y'^2 \le \rho_2^2 \, \delta^2 \\ 0, & \text{otherwise} \end{cases} \quad (31)$$

Substituting (29), (30) and (31) into (28),

$$m(x_1,y_1) = A \int_{-\infty}^{\infty} \int_{-\infty}^{\infty} \int_0^\infty L_\lambda(x_1-x', \; y_1-y', \; \theta', \; \phi')\left[S_\lambda(\chi,\psi)I_1(x',y') \cos \chi\right]$$

$$\frac{\cos\theta' \quad \sin\theta}{\rho^2} d\lambda \; dx' \; dy' \quad (32)$$

Over the footprint A_1',

$$\sin\theta = \sin(\theta_1-\alpha) = \sin\theta_1 \cos\alpha - \cos\theta_1 \sin\alpha \simeq \sin\theta_1, \quad (33)$$

$$\theta' \simeq \theta_1', \; \phi' \simeq \phi_1', \; \rho \simeq \rho_2. \quad (34)$$

With these approximations,

$$m(x_1,y_1) = \frac{A \cos\theta_1' \sin\theta_1}{\rho_2^2} \int_{-\infty}^{\infty} \int_{-\infty}^{\infty} \int_0^\infty L_\lambda(x_1-x', \; y_1-y', \; \theta', \; \phi')$$

$$\left[S_\lambda(\chi,\psi)I_1(x',y') \quad \cos\chi\right] d\lambda dx'dy' \quad (35)$$

To obtain (35) as a convolution, it is necessary to separate the wavelength, λ, from the other variables. Thus, we assume that the spectral radiance at the top of the atmosphere admits a spectral-directional model of the form

$$L_\lambda(x, y, \theta', \phi') = \frac{1}{\pi} M(x,y) R_\lambda(\theta', \phi'), \tag{36}$$

where $M(x,y)$ is the radiant exitance at the point (x,y) at the top of the atmosphere. It may be noted that the desired form (convolution) can be obtained with models somewhat more generalized than the one shown in (36); however, these generalizations will not be pursued here. We further assume that the spectral and angular characteristics of the sensor are independent of each other; i.e.,

$$S_\lambda(\chi,\psi) = S_\lambda \; S(\chi,\psi). \tag{37}$$

Rearranging (25) in terms of x', y'

$$\chi(x', y') \simeq \sin^{-1} \frac{1}{\rho_2} \{\sin^2\theta_1 \; x'^2 + \cos^2\theta_1' \; y'^2\}^{\frac{1}{2}} \tag{38}$$

Similarly, it can be shown that the angle ψ is also a function of x' and y'. Substituting the expressions for χ and ψ, we define

$$S_1(x', y') = S(\chi(x',y'), \psi(x',y')) \; I_1(x',y') \cos\chi(x',y'). \tag{39}$$

Substituting (36), (37) and (39) into (35),

$$m(x_1,y_1)=\frac{A\cos\theta_1'\sin\theta_1}{\rho_2^2}\int_{-\infty}^{\infty}\int_{-\infty}^{\infty}\int_0^{\infty}\frac{1}{\pi}M(x_1-x',y_1-y')R_\lambda(\theta_1',\phi_1')S_\lambda$$

$$S_1(x',y')\,d\lambda dx'dy' \tag{40}$$

$$m(x_1,y_1) = K_1\int_{-\infty}^{\infty}\int_{-\infty}^{\infty}M(x_1-x',\ y_1-y')S_1(x',y')dx'dy' \tag{41}$$

$$K_1 = \frac{A\cos\theta_1'\sin\theta_1}{\pi\rho_2^2}\int_0^{\infty}S_\lambda\ R_\lambda(\theta_1',\phi_1')d\lambda. \tag{42}$$

Thus, it is seen that $m(x_1,y_1)$ can be obtained (approximately) by a convolution as shown in (41). However, K_1 and S_1 still depend on the scan point (x_1,y_1). Thus, consider a "patch" about the point (x_0,y_0) such that for any scan point (x_1,y_1) on the patch

$$\sin\theta_1 \simeq \sin\theta_0,\ \theta_1' \simeq \theta_0',\ \ \phi_1' \simeq \phi_0',\ \ \rho_2 \simeq \rho_0 \tag{43}$$

Then, for any point (x_1,y_1) on the patch

$$K_0 = \frac{A\cos\theta_0'\sin\theta_0}{\pi\rho_0^2}\int_0^{\infty}S_\lambda\ R_\lambda(\theta_0',\phi_0')\,d\lambda, \tag{44}$$

$$m(x_1,y_1)=K_0\int_{-\infty}^{\infty}\int_{-\infty}^{\infty}M(x_1-x',\ y_1-y')\ S_0(x',y')dx'dy' \tag{45}$$

Thus, (45) is the desired form for the measurements, showing that a narrow field-of-view scanner can be interpreted as a linear, spatially invariant system where $S_0(x',y')$ is the point spread function of the system. It is of interest to note that the point spread function is composed of two parts. The effect of the field of view is incorporated by $I_0(x',y')$ which vanishes except for

points within the field of view. It should be noted that the effect of the partially obstructed field of view can be included by appropriate choice of $I_0(x', y')$. The angular characteristics of the detector are incorporated by the product $S(\chi, \psi) \cos\chi$. Ideally, $S(\chi,\psi)$ would be constant, at least over the field of view; and, for a narrow field-of-view sensor, $\cos\chi \simeq 1$. Thus, for an ideal sensor, the point spread function would be consant for points within the field of view and zero for other points.

It should be noted that, in terms of the coordinates x', y', the point spread function $S_0(x',y')$ varies according to the patch considered. For the circular field of view considered, it can be seen from (31) that the footprint will be circular at nadir, but will become elliptical at other points, depending on the colatitude of the patch considered. Furthermore, note that the conditions required for a patch (Eq. (43)) are independent of the longitude ϕ_0, or equivalently x_0, but depend on the colatitude θ_0. Thus, a patch could be defined as an annular surface between two equal latitude curves.

A further point of interest is the time dependence of the radiant exitance, say $M_0(x, y, t)$, at the top of the atmosphere. Suppose that at time t, the scan point is given by $(x(t), y(t))$, and define

$$M(x(t), y(t)) \triangleq M_0(x(t), y(t), t). \tag{46}$$

If the change in the radiant exitance during the time required for the satellite to move a distance corresponding to its field of

view is negligible, then (45) remains unchanged when M is defined by (46).

$$m(x_1(t),\ y_1(t)) = K_0 \int_{-\infty}^{\infty} \int_{-\infty}^{\infty} M(x_1(t)-x'\ y_1(t)-y')\ S_0(x',y')\ dx'dy'. \qquad (47)$$

Thus, the convolution remains unchanged, and the time dependence of the signal m can now be seen explicitly in (47).

A. Aliasing Error Model

The block diagram in Fig. 2 shows the main components of the ERBE NFOV scanner which is then followed by a reconstruction of the sampled signal. Thus, the radiant exitance M(x,y) at the top of the atmosphere passes through a lens and heats the detector, thus altering its temperature. The change in the temperature is sensed and converted to an electrical signal which is amplified and passed through an electrical filter to reduce the noise due to the detector and aliasing error, before being sampled, digitized and transmitted to earth by telemetry. The sampled signal is then reconstructed to obtain a continuous signal. In most cases, due to limitations in the telemetry transmission rate and the frequency content of the signals, the reconstructed signal differs from the original one; this is referred to as insufficient sampling. The error in the reconstructed signal is called aliasing noise or

error. In general, the smaller the sampling interval, the less the aliasing error introduced. However, as can be seen from the results (see section III) the choice of design parameters such as the shape of the detector field of view, the electrical filter, the use of a stepping or a continuous scan system, etc., is of considerable importance in reducing the aliasing error. Furthermore, the reduction in aliasing error obtained as the sampling interval is reduced is not uniform; so that in some instances a small reduction in the sampling interval can reduce the aliasing error noticeably more at some points than at others. Thus, in order to make the trade-off between design considerations (cost, complexity, etc.) and aliasing error, it is necessary to make a parametric quantitative study of the relationships between the various parameters involved.

It has been shown (Eq. (45)) that the effect of the detector can be expressed by a linear space-invariant system, so that the output can be described as a convolution of the input with the point spread function of the system. To establish the notation which will be used, let $g(x,y)$ be an integrable function; then its Fourier transform $\hat{g}(\nu,\omega)$ is given by

$$\hat{g}(\nu,\omega) = \int_{-\infty}^{\infty}\int_{-\infty}^{\infty} g(x,y)\, e^{-i2\pi(\nu x+\omega y)}\, dxdy. \tag{48}$$

$$g(x,y) = \int_{-\infty}^{\infty}\int_{-\infty}^{\infty} g(\nu,\omega)\, e^{i2\pi(\nu x+\omega y)}\, d\nu d\omega. \tag{49}$$

In these expressions, $g(x,y)$ can also be interpreted as a second

order stationary (i.e., homogeneous and isotropic) random process; for a more detailed treatment of these definitions, see Appendix A. It is well-known that the Fourier transform is linear and that the transform of a convolution is the product of the transforms of the convolution components [12], [13]. Thus, the transform of the detector output given by (45) is given by

$$\hat{m}(\nu,\omega) = \hat{M}(\nu,\omega)\ \hat{\tau}_d(\nu,\omega), \tag{50}$$

where $\hat{M}(\nu,\omega)$ is the transform of the radiant exitance at the top of atmosphere and $\hat{\tau}_d(\nu,\omega)$ the transform of the point spread function $\tau_d(x,y)$ defined as

$$\tau_d(x,y) = K_0\ S_0(x,y); \tag{51}$$

we will refer to $\hat{\tau}_d(\nu,\omega)$ as the frequency response of the detector. The effect of the lens has been neglected in (50), as the diffraction-limited spatial frequency response of the lens does not usually affect the frequency response of relatively low-resolution radiometers. Simulations, including the lens frequency response, during the early stages of this study, also led to the above conclusion. Thus, the effects of the lens will be neglected in the following.

In a step-scan system, the output of the detector is effectively sampled by the stepping process; i.e., if the scan points are (x_j,y_k), then the output of the radiometer at these points is $m(x_j,y_k)$. Thus, after a period is allowed for transient effects to die out, the detector output can be sampled, digitized and transmitted to ground.

When a continuous scan system is used, the detector output is amplified, then passed through a low-pass electrical filter before it is sampled. The low-pass filter serves two purposes: to reduce the amount of noise, and to lower the high frequency content of the signal before it is sampled, thus reducing aliasing error. Hence, a continuous-scan system provides a method of reducing both noise and aliasing error which is not available in step-scan systems. The amplifier gain will be assumed to be unity, for simplicity. Now, if the scanning speed is much faster than the along-track speed, then the time rate of change of the detector output follows the variations along the scan direction. In fact, let $h_e(t')$ be the impulse response of the low-pass filter; then the output of the filter can be expressed as

$$s(x(t),\ y(t)) = \int_{-\infty}^{\infty} h_e(t')\ m(x(t-t'),\ y(t-t'))\ dt' \tag{52}$$

$$\simeq \int_{-\infty}^{\infty} h_e(t')\ m(x(t),\ y(t-t'))\ dt' \tag{53}$$

$$= \int_{-\infty}^{\infty} h_e(t')\ m(x(t),\ \dot{y}t-\dot{y}t')\ dt' \tag{54}$$

$$= \int_{-\infty}^{\infty} \tau_e(y')\ m(x(t),\ y(t)-y')\ dy' \tag{55}$$

where $\dot{y}$ is the scanning speed, and

$$y(t) = \dot{y}t \quad , \quad y' = \dot{y}t', \tag{56}$$

$$\tau_e(y') = h_e(y'/\dot{y})/\dot{y}. \tag{57}$$

Thus, the effect of the electrical filter can be approximated by a convolution in the scan direction. Taking the Fourier transform of s(x,y), we obtain

$$\hat{s}(\nu,\omega) = \hat{\tau}_d(\nu,\omega)\ \hat{\tau}_e(\omega)\ \hat{M}(\nu,\omega) = \hat{\tau}(\nu,\omega)\ \hat{M}(\nu,\omega), \tag{58}$$

where $\hat{\tau}(\nu,\omega)$ is the combined frequency response or MTF of the radiometer till the filter output. Note that the effect of the lens results in the MTF

$$\hat{\tau}(\nu,\omega) = \hat{\tau}_l(\nu,\omega)\ \hat{\tau}_d(\nu,\omega)\ \hat{\tau}_e(\omega). \tag{59}$$

The output of the filter is then sampled uniformly in time, corresponding to sampling intervals X and Y along the x and y directions, respectively. This results in samples of the form $s(x_j,y_k)$; we denote the sampled signal by s(x,y; X,Y). The Fourier transform of the sampled signal is then given by

$$\hat{s}(\nu,\omega;\ X,Y) = \sum_{j=-\infty}^{\infty} \sum_{k=-\infty}^{\infty} \hat{s}\left(\nu - \frac{j}{X},\ \omega - \frac{k}{Y}\right) \tag{60}$$

$$= \sum_{j=-\infty}^{\infty} \sum_{k=-\infty}^{\infty} \hat{\tau}\left(\nu - \frac{j}{X},\ \omega - \frac{k}{Y}\right) \hat{M}\left(\nu - \frac{j}{X},\ \omega - \frac{k}{Y}\right). \tag{61}$$

If the Wiener spectrum (or power spectral density) of the radiant exitance is denoted by $\hat{\phi}_M(\nu,\omega)$, then the Wiener spectra $\hat{\phi}_s(\nu,\omega)$ and $\hat{\phi}_s(\nu,\omega;\ X,Y)$ of s(x,y) and s(x,y; X,Y), resp., are given by

$$\hat{\phi}_s(\nu,\omega) = |\hat{\tau}(\nu,\omega)|^2\ \hat{\phi}_M(\nu,\omega) \tag{62}$$

$$\hat{\phi}_s(\nu,\omega;\ X,Y) = \sum_{j=-\infty}^{\infty} \sum_{k=-\infty}^{\infty} \hat{\phi}_s\left(\nu - \frac{j}{X},\ \omega - \frac{k}{Y}\right) \tag{63}$$

$$= \hat{\phi}_s(\nu,\omega) + \hat{\phi}_a(\nu,\omega;\ X,Y). \tag{64}$$

It is seen that the spectra of the sampled signal and the continuous signal differ by the aliasing error spectrum $\hat{\phi}_a(\nu,\omega;\ X,Y)$. Under sufficient sampling conditions, the aliasing term vanishes, and it is possible to reconstruct the continuous signal from its samples with no error. When insufficient sampling occurs, this term is non-zero, and any reconstruction contains errors [14], [18].

Consider the reconstruction

$$r(x,y) = \sum_{j=-\infty}^{\infty} \sum_{k=-\infty}^{\infty} s(x_j,y_k)\ \mathrm{sinc}\frac{x-jX}{X}\ \mathrm{sinc}\frac{y-kY}{Y} \tag{65}$$

which corresponds to the reconstruction filter with frequency response

$$\hat{\tau}_R(\nu,\omega) = \Pi(X\nu,\ Y\omega) = \begin{cases} 1 & , \quad |X\nu| < \tfrac{1}{2}, |Y\omega| < \tfrac{1}{2} \\ 0 & , \quad \text{otherwise} \end{cases} \tag{66}$$

From the sampling Theorem [18], it follows that

$$\hat{r}(\nu,\omega) = \hat{\tau}_R(\nu,\omega)\ \ \hat{s}(\nu,\omega;\ X,Y) \tag{67}$$

$$= \hat{\tau}_R(\nu,\omega)\ \hat{s}(\nu,\omega) + \hat{\tau}_R(\nu,\omega)\ \hat{s}_a(\nu,\omega;\ X,Y) \tag{68}$$

$$= \hat{r}_s(\nu,\omega) + \hat{r}_a(\nu,\omega;\ X,Y). \tag{69}$$

Taking the inverse Fourier transform of (69)

$$r(x,y) = r_s(x,y) + r_a(x,y). \tag{70}$$

It is seen that the reconstruction contains a part that is due directly to the signal, and a part that is not desired, called the aliasing error. In fact, it can be shown that if $M(x,y)$ is a (real) gaussian process, then the signal and aliasing parts of the reconstruction are statistically independent and stationary processes (see Appendix A, Th. 3). Thus, the aliasing error term can be treated as additive noise.

If the useful frequency band of the signal before sampling $s(x,y)$ is considered to be $B = \{(\nu,\omega) \mid |X\nu| < \frac{1}{2}, |Y\omega| < \frac{1}{2}\}$, then, with $\hat{\tau}_R(\nu,\omega)$ given by (66), $r_s(\nu,\omega)$ is precisely the useful part of the signal. Now, since $r_s(x,y)$ and $r_a(x,y)$ are stationary processes, their variances do not change with the position (x,y).

$$\sigma_s^2 = E(r_s^2(x,y)) = \int_{-\infty}^{\infty}\int_{-\infty}^{\infty} |\hat{\tau}_R(\nu,\omega)|^2 \, \hat{\phi}_s(\nu,\omega) \, d\nu d\omega \tag{71}$$

$$= \int_{-1/2X}^{1/2X}\int_{-1/2Y}^{1/2Y} \hat{\phi}_s(\nu,\omega) \, d\nu d\omega \tag{72}$$

$$\sigma_a^2 = E(r_a^2(x,y)) = \int_{-\infty}^{\infty}\int_{-\infty}^{\infty} |\hat{\tau}_R(\nu,\omega)|^2 \, \hat{\phi}_a(\nu,\omega;\, X,Y) \, d\nu d\omega \tag{73}$$

$$= \int_{-1/2X}^{1/2X}\int_{-1/2Y}^{1/2Y} \hat{\phi}_a(\nu,\omega;\, X,Y) \, d\nu d\omega \tag{74}$$

where E denotes the statistical expectation operator. Due to the independence of the components of $r(x,y)$,

$$\sigma_r^2 = E(r^2(x,y)) = \sigma_s^2 + \sigma_a^2 \tag{75}$$

Now, note that the effect of the detector is one of averaging or low-pass filtering (e.g., see (28), (45)). Although this is

necessary to preserve a practical signal-to-noise ratio, it produces some loss in resolution, or blurring. Similarly, the electrical filter which reduces the amount of additive aliasing noise also produces some blurring due to its averaging effect. Thus, there is a trade-off between blurring and additive noise (aliasing, detector and electronic). The selection of design parameters must, therefore, be made so that both the loss of resolution as well as the additive errors (accuracy) remain within acceptable limits.

To find a quantitative means for judging the amount of blurring, note that, in the frequency domain, the loss of resolution occurs when the higher frequency content of the signal is attenuated, which in turn reduces aliasing error.

$$\sigma_M^2 = E(M^2(x,y)) = \int_{-\infty}^{\infty}\int_{-\infty}^{\infty} \hat{\phi}_M(\nu,\omega)\ d\nu d\omega, \tag{76}$$

$$\sigma_s^2 = E(r_s^2(x,y)) = \int_{-\infty}^{\infty}\int_{-\infty}^{\infty} |\hat{\tau}_R(\nu,\omega)\hat{\tau}(\nu,\omega)|^2\ \hat{\phi}_M(\nu,\omega)\ d\nu d\omega. \tag{77}$$

Thus, σ_s^2 is the variance that remains in the signal part of the reconstruction, whereas σ_M^2 is the variance of the original signal. Hence, the ratio σ_s/σ_M provides an indication of the amount of variance still remaining in $r_s(x,y)$. When the total frequency response $\hat{\tau}_R(\nu,\omega)\hat{\tau}(\nu,\omega)$ is real, monotonically non-increasing, and no greater than unity in absolute value, this ratio provides a useful measure of blurring. A more general measure of blurring can be obtained as follows. Define blurring as the difference between the

original signal and the portion of the reconstruction due to the original signal, i.e.,

$$b(x,y) = r_s(x,y) - M(x,y) \tag{78}$$

Then,

$$\hat{b}(\nu,\omega) = (\hat{\tau}_R(\nu,\omega)\ \hat{\tau}(\nu,\omega) - 1)\ \hat{M}(\nu,\omega) \tag{79}$$

$$\sigma_b^2 = E(b^2(x,y)) = \int_{-\infty}^{\infty}\int_{-\infty}^{\infty} |\hat{\tau}_R(\nu,\omega)\ \hat{\tau}(\nu,\omega) - 1|^2\ \hat{\phi}_M(\nu,\omega)\ d\nu d\omega \tag{80}$$

Note that, as defined in (78), blurring is the component that would still remain when the signal is sufficiently sampled, and no aliasing noise is present.

$$\hat{r}(\nu,\omega) = \hat{M}(\nu,\omega) + (\hat{\tau}_R(\nu,\omega)\ \hat{\tau}(\nu,\omega) - 1)\ \hat{M}(\nu,\omega) + \hat{r}_a(\nu,\omega;\ X,Y) \tag{81}$$

$$r(x,y) = M(x,y) + b(x,y) + r_a(x,y) \tag{82}$$

The ratio σ_b/σ_M provides a measure of the blurring, as a percentage of the signal variance. The extent of aliasing error in the reconstruction can be compared by the ratio σ_a/σ_M. Finally, a quantity of significance is the signal-to-noise ratio σ_s/σ_a of the signal variance to aliasing noise.

It is important to note that both blurring and aliasing errors in the reconstruction depend on the particular method of reconstruction used, i.e., on the choice of $\hat{\tau}_R(\nu,\omega)$ as can be seen from (73), (77) and (80). Thus, the particular method of reconstruction

can increase or reduce the errors involved, and should be selected with appropriate care to its effects on blurring and aliasing as well as other sources of error such as detector and electronic noise, uncertainty in knowledge of the sensor response parameters (the angular characteristics $S(\chi,\psi)$, the directional model $R_\chi(\theta', \phi')$ involved in $\hat{\tau}_d(\nu,\omega)$. No attempt was made, in this study, to optimize the reconstruction method. The choice of the frequency response in (66) was made as it tends to neither reduce nor increase these errors, thus providing an indication of the extent of these errors in the sampled signal. However, to see the effect of further smoothing of the signal, the following reconstruction filters were also considered

$$\hat{\tau}_{RN}(\nu,\omega) = \Pi(N\gamma\nu,\ N\gamma\omega) = \begin{cases} 1, & |N\gamma\nu| < \tfrac{1}{2},\ |N\gamma\omega| < \tfrac{1}{2} \\ 0, & \text{otherwise} \end{cases} \tag{83}$$

The corresponding reconstruction $r_N(x,y)$ is given by

$$r_N(x,y) = \frac{XY}{N^2\gamma^2} \sum_{j=-\infty}^{\infty} \sum_{k=-\infty}^{\infty} s(x_j, y_k)\ \mathrm{sinc}\frac{x-jX}{N\gamma}\ \mathrm{sinc}\frac{y-kY}{N\gamma}, \tag{84}$$

where γ is the effective diameter of the footprint. The variances of the smoothed reconstruction, $r_N(x,y)$, of the aliasing error in the smoothed reconstruction, and of the signal part of the smoothed reconstruction can be obtained in a similar way as for the unsmoothed case. Using (71), (73) and (75) we obtain

$$\bar{\sigma}^2_{sN} = E(r^2_{sN}(x,y)) = \int_{-1/2N\gamma}^{1/2N\gamma} \int_{-1/2N\gamma}^{1/2N\gamma} \hat{\phi}_s(\nu,\omega)\ d\nu d\omega \tag{85}$$

$$\bar{\sigma}^2_{aN} = E(r^2_{aN}(x,y)) = \int_{-1/2N\gamma}^{1/2N\gamma} \int_{-1/2N\gamma}^{1/2N\gamma} \hat{\phi}_s(\nu,\omega;\ X,Y)\ d\nu d\omega \tag{86}$$

$$\bar{\sigma}^2_{rN} = E(r^2_N(x,y)) = \bar{\sigma}^2_{sN} + \bar{\sigma}^2_{aN}. \tag{87}$$

Three types of detector frequency responses were considered. These correspond to apertures of Gaussian, circular and diamond shapes. The patch considered was assumed to be at nadir, and the angular characteristics of the detector were assumed to be uniform over the IFOV.

$$S(\chi,\psi) = 1\ ,\ \cos\chi \simeq 1. \tag{88}$$

Thus, the point spread function of the detector was assumed to be unity within the footprint, and zero outside the footprint, except for the Gaussian case. In order to compare, the results from different types of detectors, the point spread functions were normalized as to satisfy

$$\int_{-\infty}^{\infty} \int_{-\infty}^{\infty} \tau_d(x,y)\ dxdy = \frac{\pi}{4}\gamma^2 \tag{89}$$

for each case considered, where γ is the diameter of the footprint for the circular aperture at nadir.

$$\gamma^2 = h^2\ \delta^2 \tag{90}$$

where δ is the IFOV, in radians. The spatial frequency responses

are given below.

a) Gaussian:

$$\hat{\tau}_d(\nu,\omega) = e^{-\pi^2 a^2(\nu^2+\omega^2)} \quad , \; a = \gamma/2 \tag{91}$$

b) Circular:

$$\hat{\tau}_d(\nu,\omega) = \frac{J_1(2\pi a\rho)}{\pi a\rho} \quad , \; a = \gamma/2, \qquad \rho^2 = \nu^2 + \omega^2 \tag{92}$$

c) Diamond:

$$\hat{\tau}_d(\nu,\omega) = \mathrm{sinc}(a\nu+b\omega)\ \mathrm{sinc}(a\nu-b\omega), \quad a = \frac{\pi\gamma}{4} \; , \; b = \frac{\gamma}{2}. \tag{93}$$

Perspective plots of these frequency responses are shown in Fig. 3.

The electrical filter frequency response was selected as

$$\hat{\tau}_e(\omega) = \begin{cases} 1 - (\gamma\omega)^4 \; , & |\omega| < \frac{1}{\gamma} \\ 0 \; , & \text{otherwise} \end{cases} \tag{94}$$

Although this is not the frequency response of a causal electrical filter, it is representative of the magnitude characteristics of realizable filters. However, the phase characteristics that would introduce further blurring are not represented appropriately by this model. More realistic filters which operate in real time were modeled and coded in a simulation as rational transfer functions up to eight order, so that the capability of simulating the effects of these filters was developed.

Finally, the radiant exitance at the top of the atmosphere was modeled as a random process (or field) which is homogeneous and

isotropic, i.e., wide-sense stationary. Since the particular values of the radiant exitance at the top of the atmosphere are not known a priori, and it is desirable to design the radiometer for a large class of possible signals, it is usual and pratical to model the radiant exitance as a random process. We will consider $M(x,y)$ to represent the fluctuation of the radiant exitance about its mean value, say $\overline{M}$, as the effect of a mean value $\overline{M}$ is to introduce a mean value in the output signal of the radiometer, as can be seen by

$$\int_{-\infty}^{\infty}\int_{-\infty}^{\infty} (M(x',y') + \overline{M})\ \tau(x-x',\ y-y')\ dx'dy'$$

$$= \int_{-\infty}^{\infty}\int_{-\infty}^{\infty} M(x',y')\ \tau(x-x',y-y')\ dx'dy' + \overline{M}\iint_{-\infty}^{\infty} \tau(x',y')dx'dy' \quad (95)$$

$$= s(x,y) + \overline{s} \quad (96)$$

$$\overline{s} = \overline{M}\iint_{-\infty}^{\infty} \tau(x',y')\ dx'dy' \quad (97)$$

Since the effect of an average value can thus be taken into account, we assume that

$$E(M(x,y)) = 0 \quad (98)$$

$$\phi_M(x,y) = E(M(x_0+x,y_0+y)\ M(x_0,y_0)) = \sigma_M^2\ e^{-r/\mu_r} \quad (99)$$

$$r = (x^2+y^2)^{\frac{1}{2}}. \quad (100)$$

The Wiener spectrum corresponding to the covariance function, $\phi_M(x,y)$, is given by

$$\hat{\phi}_M(\nu,\omega) = \frac{2\pi\ \mu_r^2\ \sigma_M^2}{\left[1 + 4\pi^2\ \mu_r^2(\nu^2+\omega^2)\right]^{3/2}} \tag{101}$$

The Wiener spectrum in (101) can be obtained by assuming that $M(x,y)$ is a random set of two-dimensional pulses whose width obeys a Poisson probability law with a mean width μ_r, and whose magnitude obeys a Gaussian probability law with zero mean and variance σ_M^2 [15], [16], [17]. This interpretation provides a physical significance to the parameter μ_r. It is important to note that by varying μ_r, it is possible to distribute the frequency content of the signal with ease. As μ_r decreases, the spectrum becomes flatter, favoring the higher end of the spectrum. When σ_M^2 is kept constant, the variance of the signal remains unchanged, so that meaningful comparisons can be made. Finally, note that for the Lambertian case,

$$L_\lambda(x,\ y,\ \theta',\ \phi') = \frac{1}{\pi}\ M(x,\ y)\ R_\lambda\ , \tag{102}$$

so that the analysis for the radiance would be essentially the same if the subscript M is replaced by L; i.e., σ_M by σ_L , $\hat{\phi}_M(\nu,\omega)$ by $\hat{\phi}_L(\nu,\omega)$, etc.

B. Information Density

In situations where information in the input signal (e.g.,

the radiant exitance at the top of the atmosphere) is transmitted through a system (the radiometer) resulting in an output signal (the sampled digital radiometer output), a criterion of interest is the density of the information transmitted. This criterion, which was introduced by Shannon [18] for communication systems, was investigated for image quality considerations by Fellgett and Linfoot [19] and for aliasing effects by Huck and Park [20].

Since transmitting a signal which is known a priori does not increase our knowledge, the mathematical concept of information is based on the amount of uncertainty reduced by the transmission of a signal. The entropy [18] of a signal is a measure of the uncertainty of receiving it. For a band-limited, second order stationary, Gaussian random process, g(x,y), with Wiener spectrum $\hat{\phi}_g(\nu,\omega)$, the entropy can be shown to be [18, pp. 91 -95], [20],

$$H(g) = \frac{1}{2} \int_{-\nu_0/2}^{\nu_0/2} \int_{-\omega_0/2}^{\omega_0/2} \log_2(4\pi\, \hat{\phi}_g(\nu,\omega))\, d\nu d\omega, \tag{103}$$

where the spectrum $\hat{\phi}_g(\nu,\omega)$ is limited to the band $\{(\nu,\omega) \mid |\nu| < \nu_0/2, \quad |\omega| < \omega_0/2\}$.

In the previous section, it was shown that the reconstruction r(x,y) can be written as the sum of a signal part, $r_s(x,y)$, and an aliasing error part, $r_a(x,y)$ (see (70)). The effects of detector and electronic noise as well as quantization error effects were neglected. Now, suppose that the detector and electronic noise from the amplifier and electrical filter, referenced to the input

of the filter, are modeled by Gaussian noise. Let $n(x,y)$ be the noise added to the detector output when the scan point is (x,y). Thus, the input to the electronics can now be expressed by $m(x,y)+n(x,y)$. To simplify the formulation, we shall assume that the noise, $n(x,y)$, is white when y is kept constant and x is allowed to vary. When the temporal power spectral density function of the noise is relatively flat, or alternately, when the temporal correlation function of the noise decays rapidly (i.e., if the correlation function is almost zero in a fraction of the time required for one scan), then the assumption is realistic. Since two scan points (x_1,y) and (x_2,y) will correspond to times t_1 and t_2, respectively, separated by an interval, $t_2 - t_1$, which, on average, equals the time required for one scan, $n(x_1,y)$ and $n(x_2,y)$ will be almost uncorrelated; hence, in the x direction the noise will appear to be white. Thus, let

$$E(n(x+x',y+y')\ n(x,y)) = \phi_n(y')\ \ \delta(x') \tag{104}$$

The Wiener spectrum of the noise will then be dependent on one variable, as it is constant in ν.

$$\hat{\phi}_n(\nu,\omega) = \hat{\phi}_n(\omega). \tag{105}$$

As shown in the previous section (see (52) - (58)), the effect of the electrical filter is to process the noise only in the ω-axis. Adding the effects of sampling, A/D conversion and the reconstruction filter, the reconstructed signal can be expressed by

$$r(x,y) = r_s(x,y) + r_a(x,y) + r_n(x,y) + r_q(x,y), \tag{106}$$

where $r_n(x,y)$ and $r_q(x,y)$ are the parts of the reconstructed signal due to noise and quantization (A/D conversion) errors, respectively. The spectrum of the noise term can be found to be

$$\hat{\phi}_{r_n}(\nu,\omega) = \sum_{k=-\infty}^{\infty} \left|\tau_e(\omega-\frac{k}{Y})\right|^2 \hat{\phi}_n(\omega-\frac{k}{Y}) = \hat{\phi}_{r_n}(\omega), \quad |X\nu|<\frac{1}{2}, \quad |Y\omega|<\frac{1}{2} \tag{107}$$

If the A/D conversion consists of rounding to the nearest allowable level, and E_0 is the maximum error that can occur (except for overflow), then the quantization error can be modelled by

$$\hat{\phi}_{r_q}(\nu,\omega) = E_0^2/3. \tag{108}$$

If the digital words consist of η bits plus a sign bit, the number of allowable levels, κ, is

$$\kappa = 2^{\eta+1}$$

Finally, if the signal is expected to have a dynamic range of $\left[-M, M\right]$,

$$\hat{\phi}_{r_q}(\nu,\omega) = \frac{M^2}{3\kappa^2}, \quad E_0 = M/\kappa. \tag{109}$$

In the Appendix, it is shown that for a second order stationary real Gaussian random process, the aliasing error and signal processes are second order stationary and statistically independent. We further assume that both the quantization error and noise terms are Gaussian and statistically independent from the radiant exitance signal. The

Wiener spectrum of the reconstructed signal r(x,y) in (106), is then given by

$$\hat{\phi}_r(\nu,\omega) = \hat{\phi}_{r_s}(\nu,\omega) + \hat{\phi}_{r_a}(\nu,\omega) + \hat{\phi}_{r_n}(\nu,\omega) + \hat{\phi}_{r_q}(\nu,\omega). \tag{110}$$

For the channel described by (106), where $r_s(x,y)$ is the input signal and r(x,y) is the output, due to the statistical independence of the additive terms, it can be shown that [17, p. 99] the information density is given by

$$h_i = H(r) - H(r_a + r_n + r_q). \tag{111}$$

Using (103), and manipulating

$$h_i = \frac{1}{2} \int_{-\frac{1}{2X}}^{\frac{1}{2X}} \int_{-\frac{1}{2Y}}^{\frac{1}{2Y}} \log_2 \left[1 + \frac{\hat{\phi}_s(\nu,\omega)}{\hat{\phi}_a(\nu,\omega;X,Y) + \phi_{r_n}(\omega) + M^2\kappa^{-2}/3} \right] d\nu d\omega \tag{112}$$

$$\hat{\phi}_s(\nu,\omega) = |\hat{\tau}(\nu,\omega)|^2 \phi_M(\nu,\omega), \tag{113}$$

$$\hat{\phi}_a(\nu,\omega;X,Y) = \sum_{\substack{j=-\infty \\ (j,k)\neq(0,0)}}^{\infty} \sum_{k=-\infty}^{\infty} \left| \hat{\tau}(\nu - \tfrac{j}{X}, \omega - \tfrac{k}{Y}) \right|^2 \hat{\phi}_M(\nu - \tfrac{j}{X}, \omega - \tfrac{k}{Y}). \tag{114}$$

Note that when the cut-off frequency of the low-pass electrical filter is chosen so as to attenuate the frequency content outside the Nyquist band significantly, the aliased portion of the noise becomes small relative to the portion of noise within the passband; i.e.,

$$\sum_{\substack{k=-\infty \\ k\neq 0}}^{\infty} \left|\tau_e(\omega-\frac{k}{Y})\right|^2 \hat{\phi}_n(\omega-\frac{k}{Y}) << \left|\tau_e(\omega)\right|^2 \hat{\phi}_n(\omega), \quad |Y\omega| < \frac{1}{2} \tag{115}$$

$$\hat{\phi}_{r_n}(\nu,\omega) \simeq \left|\hat{\tau}_e(\omega)\right|^2 \hat{\phi}_n(\omega). \tag{116}$$

Thus, the information density transmitted through the system can be computed using (112) - (116). To see the effect of specific parameters more explicitly, consider the following normalizations:

$$\hat{\phi}_M(\nu,\omega) = \sigma_M^2 \hat{\phi}'_M(\nu,\omega), \quad \hat{\phi}'_n(\omega) = \sigma_n^2 \hat{\phi}'_n(\omega), \tag{117}$$

$$\hat{\tau}(\nu,\omega) = K_\tau \hat{\tau}'(\nu,\omega), \quad \hat{\tau}_e(\omega) = K_e \hat{\tau}'_e(\omega), \tag{118}$$

where the prime " ' " denotes a normalized quantity, K_τ is the total "d-c" gain of the radiometer system, K_e the d-c gain of the electronics, σ_M^2 and σ_n^2 the variances of the input signal and the noise, respectively. Substituting these expressions into (112),

$$h_i = \frac{1}{2} \int_{-\frac{1}{2X}}^{\frac{1}{2X}} \int_{-\frac{1}{2Y}}^{\frac{1}{2Y}} \log_2 \left[1 + \frac{\left|\hat{\tau}'(\nu,\omega)\right|^2 \hat{\phi}'_M(\nu,\omega)}{\hat{\phi}'_a(\nu,\omega;X,Y) + \left(\frac{\sigma_M}{\sigma_n}\right)^{-2}\left(\frac{K_\tau}{K_e}\right)^{-2} \left|\hat{\tau}'_e(\omega)\right|^2 \hat{\phi}_n(\omega) + \frac{M^2\kappa^{-2}}{3\sigma_M^2 K_\tau^2}} \right] d\nu d\omega \tag{119}$$

The expression in (119) shows the dependence of the information density on various system parameters explicitly. For example, if the total system gain, K_τ, is increased by increasing the electronic amplification K_e (i.e., K_τ/K_e remains unchanged), the information density would remain unchanged, assuming that the dynamic range of the signal

increases proportionately. On the other hand, if K_τ is increased by increasing the gain of the detector or the lens configuration, the effect of the noise would be reduced, while the aliasing error term would remain unchanged, assuming σ_n remains unchanged. To see this more clearly, let $\sigma_{s/n}$ be the signal to noise ratio of the input signal (radiant exitance) to the noise (detector plus electrical) both referenced at the output of the detector; then

$$\sigma_{s/n} = \frac{K_\tau}{K_e} \sigma_M/\sigma_n. \tag{120}$$

On the other hand, the standard deviation of the signal at the input of the A/D converter is

$$\sqrt{\sigma_M^2 K_\tau^2 + \sigma_n^2 K_e^2} \simeq \sigma_M K_\tau, \text{ if } \sigma_{s/n}^2 >> 1. \tag{121}$$

Since the dynamic range of this signal would be directly proportional to its standard deviation, let

$$M = c\, \sigma_M K_\tau \tag{122}$$

Substituting (120) and (122) into (119),

$$h_i = \frac{1}{2} \int_{-\frac{1}{2X}}^{\frac{1}{2X}} \int_{-\frac{1}{2Y}}^{\frac{1}{2Y}} \log_2 \left[1 + \frac{|\hat{\tau}'(\nu,\omega)|^2 \hat{\phi}_M'(\nu,\omega)}{\hat{\phi}_a'(\nu,\omega;X,Y) + \sigma_{s/n}^{-2} |\hat{\tau}_e'(\omega)|^2 \hat{\phi}_n'(\omega) + \frac{c^2}{3} \kappa^{-2}} \right] d\nu d\omega \tag{123}$$

It is seen that the combined effects of the gains and σ_M, σ_n can be combined into the parameter $\sigma_{s/n}$; i.e., the signal to noise ratio referenced at the detector output. The effects of shaping the transfer

functions $\hat{\tau}'(\nu,\omega)$ and $\hat{\tau}_e(\omega)$ are less explicit and have been investigated in the previous section for aliasing and blurring. The effect of the sampling intervals is shown in Figure 10.

III. RESULTS

The models described in section II were used to make a parametric study of the effects of various design parameters such as aperture shape, continuous versus step scan, sampling interval, etc., on aliasing error. A computer program which computes the variance of the signal and aliasing error, and signal-to-noise ratio was developed. The program generates the Wiener spectrum of the optical signal, the frequency response of the lens, the frequency response of the selected detector aperture shape, and the transfer function of the electrical filter. Then, using these functions, the Wiener spectra of the continuous and sampled radiometer output are computed. The spectrum of the sampled signal was generated by including the effects of the eight sidebands closest to the fundamental band at the origin, as these have the largest effect on the spectrum, while further sidebands have negligible effect within the reconstruction band $\{(\nu,\omega) \mid \ |X\nu| < \frac{1}{2},\ |Y\omega| < \frac{1}{2}\}$. In all the runs made the sampling intervals in the along-track and scan directions, x and y respectively, were chosen to be equal; i.e., $X = Y$.

To obtain results which are useful in a more general context, the independent variables x and y were normalized by the diameter, γ, of the effective circular footprint. Thus, the values $X/\gamma=Y/\gamma=1$ correspond to the contiguous sampling case for a circular IFOV,

irrespective of the particular value of γ. Similarly, the average pulse width of the signal is also normalized, so that the normalized parameter μ_r/γ represents the average number of zero-crossings occurring within the footprint. To make the results applicable to different levels of signal power, the variances of the signal and aliasing error were computed as ratios of the variance of the incoming radiant exitance. As the system is linear, any particular signal level can be readily obtained from the ratios. The integrals required to compute the variances of the signal and aliasing error (e.g., (72), (74)) were evaluated using simple numerical integration techniques.

Figure 6 shows the normalized variances of the signal and aliasing error components of the reconstruction given in (65) and (70) and the signal-to-noise ratio as a function of the normalized sampling interval X/γ, various Wiener spectra as input radiant exitance; the spectra are parametrized by μ_r/γ. The three cases shown correspond to the Gaussian aperture with step-scan, the circular aperture with step-scan, and the diamond aperture with continuous scan.

Figure 7 shows the normalized variance of the aliasing error in the smoothed reconstruction given in (84) and the signal-to-noise ratio as a function of the normalized sampling interval for varying amount of smoothing indexed by N.

Figure 8 shows the aliasing error variance and the signal-to-noise ratio for the smoothed reconstruction when continuous scan,

hence electrical filtering, is used. To see the effect of continuous versus step-scan to aliasing error, compare with Figure 7.

Figure 9 shows the normalized variances of the signal and aliasing error parts of the smoothed reconstructions, and the signal-to-noise ratio as a function of the frequency content of the input radiant exitance indexed by μ_r/γ. It is seen that while smoothing reduces aliasing error, it also increases blurring as measured by σ_s/σ_L.

Figure 10 shows the information density transmitted through the radiometer for the unsmoothed reconstruction as a function of the normalized sampling interval. Plots for a radiant exitance Wiener spectrum corresponding to white noise with unit power, as well as various levels of coloring are given. Note that the white noise spectrum has infinite variance, so that the results are not readily comparable.

IV. CONCLUSIONS

1. The numerical results substantiate the observation by Mertz and Grey [2] and Schade [3] that all reasonable spot intensity profiles and photosensor aperture shapes of equivalent size result in about equal blurring, but that some profiles and shapes tend to suppress aliasing better than others. The Gaussian spot intensity profile of television cameras is appreciably superior to the circular photosensor aperture commonly used in optical-mechanical scanners. However, aliasing with optical-mechanical scanners can be effectively suppressed by careful photosensor aperture and electronic filter response shaping.

2. Aliasing errors can be the most significant source of degradation in contiguous reconstructions of a discrete signal. Consider, for example, a discrete signal from an optical-mechanical scanner with a circular photosensor aperture and contiguous coverage (i.e., $X/\gamma = Y/\gamma = 1$), and a random radiance fluctuation with a mean spatial detail equal to the sampling interval (i.e., $\mu_r/\gamma' = 1$). The resulting rms signal-to-noise ratio σ_s/σ_a is then only 5, whereas imaging systems and radiometers are commonly designed to provide signal-to-noise ratios of two to three orders of magnitude in typical applications.

3. Aliasing errors tend to decrease rapidly with decreasing sampling intervals. Improvements of one or two orders of magnitude,

depending on the spot intensity profile or aperture shape, can be attained by decreasing the sampling intervals $X/\gamma = Y/\gamma$ from 1 to 0.7. Still further decreases in sampling intervals continue to provide rapid improvements for the Gaussian profile, but relatively gradual improvements for the circular and diamond apertures. This difference in performance between the Gaussian profile and the two apertures is directly attributable to their frequency response characteristics: the frequency response of the Gaussian profile decreases monotonically with frequency, whereas the frequency response of the two apertures exhibit sidelobes. The reason for the improved performance of the diamond over the circular aperture is that the sidelobes of the diamond aperture are suppressed along the two sampling directions (i.e., by its shape along the ω-direction and by an electronic filter along the ν- direction).

4. The improvements that can be attained in suppressing aliasing by photosensor aperture shaping and decreasing the sampling interval tend to be independent of the statistical properties of the radiance fluctuation.

5. Spatially smoothed reconstructions reduce aliasing error at the cost of increased blurring. But there is a net loss in signal-to-noise ratio (i.e., $\bar{\sigma}_s/\bar{\sigma}_a \lesssim \sigma_s/\sigma_a$), and hence loss of information about spatial detail. This suggests that the passband of the reconstruction filter should generally be equal to the sampling passband. Narrower reconstruction filters (i.e.,

smoothed reconstructions) should be used only if spatial detail is of secondary importance to the accurate estimation of absolute radiance magnitudes of coarse detail (as it is commonly in the reconstruction of radiometric measurements).

APPENDIX A

SAMPLING OF SECOND ORDER STATIONARY RANDOM PROCESSES

Consider a second order random process $\{x(t), -\infty < t < \infty\}$, defined on a fixed probability space (Ω, A, P). Let

$$E(x(t)) = 0 \tag{1}$$

$$E(x(t)x^*(t')) = R_x(t,t'). \tag{2}$$ [1]

Suppose that the random process is sampled at intervals T, to obtain the sequence $\{x(kT), -\infty < k < \infty\}$. Whatever the physical nature of the sampled process (whether a sequence of numbers stored in a computer, the output of a sample-hold device, etc.), it contains information about the continuous process x(t). In many practical applications, it is desirable to obtain a continuous random process, $x_r(t)$, from the samples of another random process, x(t), such that $x_r(t)$, resembles x(t) is some fashion; e. g., $E|x(t) - x_r(t)|^2$ is small or minimum. Such a process, $x_r(t)$, will be called a reconstruction of x(t). In the following, we shall assume that the random processes considered have zero mean without loss of generality, as the mean (if finite) can be subtracted.

Def. 1

A random process is said to be second order stationary (or wide sense stationary) if it is of second order and its covariance

---

[1] * denotes the complex conjugate.

depends only on the difference of its arguments, i. e.,

$$E(x(t+\tau)x^*(t)) = R_x(\tau), \quad t, \tau \varepsilon R.^2 \tag{3}$$

Second order stationary processes have harmonic (or spectral) decompositions as stated in the following theorem (for a proof see Loève [21], pp. 474 - 483).

Theorem 1

A second order random process $x(t)$ with $t \varepsilon R$ has a harmonic orthogonal decomposition

$$x(t) = \int_{-\infty}^{\infty} e^{i\omega t} dX(\omega) \tag{4}$$

where $\{X(\omega), \omega \varepsilon R\}$ is a process with orthogonal increments such that whenever $\omega_1 \leq \omega_2$

$$E|X(\omega_2) - X(\omega_1)|^2 = F(\omega_2) - F(\omega_1), \tag{5}$$

and $F(\omega)$ is of bounded variation if, and only if, $x(t)$ is second order stationary and continuous in quadratic mean (q.m.) at one point. Then,

$$\underset{\tau \to \infty}{\text{l.i.m.}} \frac{1}{2\tau} \int_{-\tau}^{\tau} x(t) e^{-i\omega t} dt = X(\omega+) - X(\omega-) \tag{6}$$

$$\underset{\tau \to \infty}{\text{l.i.m.}} \frac{1}{2\pi} \int_{-\tau}^{\tau} x(t) \frac{e^{-i\omega t} - e^{-i(\omega+h)t}}{it} dt = \hat{X}(\omega+h) - \hat{X}(\omega), \tag{7}$$

$$\hat{X}(\omega) = \frac{1}{2}\left[X(\omega+) + X(\omega-)\right]. \tag{8}$$

---

[2] R denotes the real numbers

The theorem remains valid if the argument t is restricted to the integers, the continuity of x(t) is deleted, and the integrals in (6), (7), are replaced by appropriate sums.

The stochastic integrals above should be interpreted as Riemann-Stieltjes integrals in q.m. (see Loève [21], p. 472), and l.i.m. denotes the limit in quadratic mean.

For a second order stationary process, x(t), continuous in q.m., we shall call any process $X(\omega)$ satisfying (4) an Integrated Fourier Transform (IFT) of x(t). A non-decreasing function $F(\omega)$ satisfying (5) will be called an Integrated Power Spectrum (IPS) of x(t). If $F(\omega)$ is absolutely continuous, then the derivative

$$S(\omega) = \frac{dF}{d\omega}(\omega) \tag{9}$$

is called the Power Spectral Density (PSD) of the process x(t).[3] As in the case of deterministic signals, the concepts of power spectra (or harmonic decompositions) and Fourier transforms play an important role in the analysis of random processes.

Def. 2

Let $\{x(t), t\epsilon R\}$ be a second order random process, and $\{t_k, k = \ldots, -1, 0, 1, \ldots\}$ an increasing sequence of sampling

[3] More generalized definitions applicable to non-stationary process are possible and will be studied later.

points. Then $\{x_r(t),\ t\varepsilon R\}$ is a real (complex) linear reconstruction of $x(t)$ if there are real (complex) functions $u_k(t)$ such that

$$x_r(t) = \underset{n\to\infty}{\text{l.i.m.}} \sum_{k=-n}^{n} x(t_k)u_k(t) \triangleq \sum_{k=-\infty}^{\infty} x(t_k)u_k(t), \quad t\varepsilon R. \tag{10}$$

In particular, if $t_k = kT$, the linear reconstruction

$$x_s(t) = \sum_{k=-\infty}^{\infty} x(kT)\ \text{sinc}(k - \tfrac{t}{T})\pi, \quad t\varepsilon R \tag{11}$$

will be called the Shannon reconstruction of $x(t)$ if the limit in (11) exists.

Note that, for the Shannon reconstruction,

$$u_k(t_j) = \delta_{kj} = \begin{cases} 1, & k = j \\ 0, & k \neq j \end{cases}, \tag{12}$$

$$x_s(t_k) = x(t_k), \quad t_k = kT. \tag{13}$$

Condition (12), which implies (13), is clearly a desirable one when trying to reduce the difference between $x(t)$ and the reconstruction.

<u>Def. 3</u>

Let $\{x(t),\ t\varepsilon R\}$ be second order stationary and continuous in q.m., with IFT $X(\omega)$. Then the kth sideband of the process for a uniform sampling interval T is

$$X_k(\omega) = X(\omega+k\omega_0) - X(k\omega_0), \quad \omega_0 = 2\pi/T, \quad k = 0, \pm 1, \ldots \tag{14}$$

The kth sideband signal of the process is

$$x_k(t) = \int_{-\omega_0/2}^{\omega_0/2} e^{i\omega t}\, dX_k(\omega), \quad t\varepsilon R, \quad k = 0, \pm 1, \ldots \tag{15}$$

Lemma 1

Let $\{x(t),\ t\varepsilon R\}$ be second order stationary and continuous in q.m. Then the sideband signals $\{x_k(t),\ t\varepsilon R\}$ are uncorrelated, second order stationary processes; the sidebands $\{X_k(\omega),\ -\omega_0/2 \le \omega < \omega_0/2\}$ are processes with orthogonal increments such that

$$E([X_k(\omega_2) - X_k(\omega_1)][X_j(\omega_4) - X_j(\omega_3)]^*) = 0,\ k \neq j \tag{16}$$

whenever $-\omega_0/2 \le \omega_1,\ \omega_2,\ \omega_3,\ \omega_4, < \omega_0/2$; and

$$E(|X_k(\omega_2) - X_k(\omega_1)|^2) = F_k(\omega_2) - F_k(\omega_1), \quad \omega_1 \le \omega_2 \tag{17}$$

$$F_k(\omega) = F(\omega + k\omega_0). \tag{18}$$

Proof:

First note that (17) follows from (14) and (5); since, whenever $\omega_1 \le \omega_2$

$$E(|X_k(\omega_2) - X_k(\omega_1)|^2) = E(|X(\omega_2+k\omega_0) - X(\omega_1+k\omega_0)|^2) \tag{19}$$

$$= F(\omega_2+k\omega_0) - F(\omega_1+k\omega_0). \tag{20}$$

Now, let $\omega_i \varepsilon [-\omega_0/2,\ \omega_0/2)$, $i = 1, 2, 3, 4$; then

$$E([X(\omega_2+k\omega_0) - X(\omega_1+k\omega_0)][X(\omega_4+j\omega_0) - X(\omega_3+j\omega_0)]^*) = 0,\ k \neq j \tag{21}$$

since $X(\omega)$ has orthogonal increments (Th. 1) and the intervals $[\min(\omega_1,\omega_2)+k\omega_0,\ \max(\omega_1,\omega_2)+k\omega_0)$ and $[\min(\omega_3,\omega_4)+j\omega_0,\ \max(\omega_3,\omega_4)+j\omega_0)$ are disjoint if $k \neq j$. Substituting (14) into (21), (16) follows.

To show that the sidebands have orthogonal increments, suppose $-\omega_0/2 \le \omega_1 \le \omega_2 \le \omega_3 \le \omega_4 \le \omega_0/2$; then

$$E([X_k(\omega_2) - X_k(\omega_1)][X_k(\omega_4) - X_k(\omega_3)]^*) = E([X(\omega_2+k\omega_0) - X\ \omega_1+k\omega_0)]$$
$$[X(\omega_4+k\omega_0) - X(\omega_3+k\omega_0)]^*) = 0 \tag{22}$$

Thus, the assertions about the sidebands have been proved. To see that the sideband signals are stationary, it suffices to note that

$$R_k(t,t') = E(x_k(t)\, x_k^*(t')) = E(\int_{-\omega_0/2}^{\omega_0/2} e^{i\omega t}\, dX_k(\omega) \int_{-\omega_0/2}^{\omega_0/2} e^{-i\omega t'}\, dX_k^*(\omega)) \tag{23}$$

$$= \int_{-\omega_0/2}^{\omega_0/2} e^{i\omega(t-t')}\, dF_k(\omega). \tag{24}$$

Thus, the covariance $R_k(t,t')$ depends only on the difference of the arguments, i.e., $t-t'$.

$$E(|x_k(t)|^2) = \int_{-\omega_0/2}^{\omega_0/2} dF_k(\omega) = F_k(\omega_0/2) - F_k(-\omega_0/2) < \infty,\ t \varepsilon R. \tag{25}$$

Hence, $x_k(t)$ is second order stationary.

Now let $k \neq j$ and $t, t' \varepsilon R$,

$$E(x_k(t)\, x_j^*(t')) = E(\int_{-\omega_0/2}^{\omega_0/2} e^{i\omega t}\, dX_k(\omega) \int_{-\omega_0/2}^{\omega_0/2} e^{-i\omega' t'}\, dX_j^*(\omega')) \tag{26}$$

$$= 0 \tag{27}$$

where (27) follows from (16) and the definition of the integral. Hence, the sideband signals are uncorrelated, and the lemma is proved.

Def. 4

Let $\{x(t),\ t\varepsilon R\}$ be second order stationary and continuous in q.m. with IFT $X(\omega)$. Then the kth two-sided sideband is

$$\overline{X}_k(\omega) = X_k(\omega) + X_{-k}(\omega), \quad k = 0, \pm 1, \pm 2, \ldots . \tag{28}$$

The kth two-sided sideband signal is

$$\overline{x}_k(t) = x_k(t) + x_{-k}(t), \quad k = 0, \pm 1, \pm 2, \ldots . \tag{29}$$

Lemma 2

Let $\{x(t),\ t\varepsilon R\}$ be second order stationary and continuous in q.m. with IFT $X(\omega)$. If $a < b$ and the complex function, f, is continuous on $[a, b]$, then

$$\int_a^b f(\omega)\,dX(\omega) = \int_a^b f(\omega)\,d\hat{X}(\omega) + f(b)\left[X(b) - \hat{X}(b)\right] - f(a)\left[X(a) - \hat{X}(a)\right] \tag{30}$$

where $\hat{X}(\omega)$ is defined by (8).

Proof:

Since $\hat{X}(\omega)$ coincides with $X(\omega)$ when ω is a continuity point (in q.m.), the second order process

$$\tilde{X}(\omega) = X(\omega) - \hat{X}(\omega) \tag{31}$$

vanishes except for a countable number of discontinuity points. Hence, $\tilde{X}(\omega)$ is zero on a set C dense in $[a, b)$. Now choose a sequence of finite partitions, P_n, of $[a, b)$, whose points lie in C with the possible exception of a and b. Since C is dense, the

sequence can be chosen so that the norm of the partitions converges monotonically to zero. Then,

$$\int_a^b f_{P_n}(\omega)\, d\tilde{X}(\omega)=F(\omega_{nn})\tilde{X}(b)-f(\omega_{1n})\tilde{X}(a), \tag{32}$$

where ω_{1n} is in the first subinterval of P_n and ω_{nn} is in the last, and $f_{P_n}(\omega)$ is the restriction of the continuous and bounded function $f(\omega)$ to P_n. Since $\omega_{1n} \to a$, $\omega_{nn} \to b$ and f is continuous,

$$\int_a^b f(\omega)d\tilde{X}(\omega)=f(b-)\tilde{X}(b)-f(a+)\tilde{X}(a). \tag{33}$$

Hence, the integral on the LHS of (33) exists; since $\int_a^b f(\omega)dX(\omega)$ exists, (see Loève [21], p. 473), then so does $\int_a^b f(\omega)d\hat{X}(\omega)$; and the assertion is proved.

In particular, note that if $X(\omega)$ is continuous in q.m. at a and b, then the last two terms in (30) vanish and the two integrals are equal [a, e]. It is also interesting to note that for a continuous integrand, if ω is an interior point of discontinuity, then the integral depends on the jump $X(\omega+)-X(\omega-)$, but does not depend on $X(\omega)$, as evidenced by the preceding lemma.

Lemma 3

Let $\{x(t),\ t\epsilon R\}$ be second order stationary and continuous in q.m. with IFT $X(\omega)$. Then, the second order process $\overline{X}(\omega)$, defined by

$$\overline{X}(\omega) = \begin{cases} X(\omega-) \ , & \omega \geq 0 \\ X(\omega+) \ , & \omega < 0 \end{cases} \tag{34}$$

has orthogonal increments; furthermore,

$$x(t) = \int_{-\infty}^{\infty} e^{i\omega t} d\overline{X}(\omega), \quad t \varepsilon R \tag{35}$$

Proof:

Consider four points on the real line such that $-\infty < \omega_1 < \omega_2 \leq \omega_3 < \omega_4 < \infty$. It is necessary to show that

$$E([\overline{X}(\omega_4)-\overline{X}(\omega_3)][\overline{X}(\omega_2)-\overline{X}(\omega_1)]^*) = 0 \tag{36}$$

First let $\omega_3 \geq 0$, then

$$\overline{X}(\omega_4)-\overline{X}(\omega_3)=X(\omega_4-)-X(\omega_3-)= \underset{h \downarrow 0}{\text{l.i.m.}} X(\omega_4-h)-X(\omega_3-h) \tag{37}$$

Now, if $\omega_2 \geq 0$, then

$$\lim_{h\downarrow 0} E([X(\omega_4-h)-X(\omega_3-h)][X(\omega_2-h)-X(\omega_1 \pm h)]^*) = 0, \tag{38}$$

if $\omega_2 < 0$, then

$$\lim_{h\downarrow 0} E([X(\omega_4-h)-X(\omega_3-h)][X(\omega_2+h)-X(\omega_1+h)]^*) = 0, \tag{39}$$

Hence, (36) holds when $\omega_3 \geq 0$. Finally, if $\omega_3 < 0$,

$$\lim_{h\downarrow 0} E([X(\omega_4 \pm h)-X(\omega_3+h)][X(\omega_2+h)-X(\omega_1+h)]^*) = 0. \tag{40}$$

Hence, $\overline{X}(\omega)$ has orthogonal increments.

To show (35), recall that $F(\omega)$ is of bounded variation; hence, the following limits exist.

$$\underset{\omega \to \infty}{\text{l.i.m.}} X(\pm\omega) = X(\pm\infty), \tag{41}$$

$$0 \le E|X(\omega)-X(\omega-)|^2 = F(\omega)-F(\omega-) \to 0 \tag{42}$$

$$0 \le E|X(-\omega)-X(-\omega+)|^2 = F(-\omega+)-F(-\omega) \to 0 \tag{43}$$

So that $\overline{X}(\pm\infty)$ can be defined as

$$\overline{X}(\pm\infty) = \underset{\omega \to \infty}{\text{l.i.m.}}\ \overline{X}(\pm\omega) = X(\pm\infty). \tag{44}$$

Since $X(\omega)$ and $\overline{X}(\omega)$ differ only on the countable set of discontinuity points, using Lemma 2,

$$\int_a^b e^{i\omega t} d\overline{X}(\omega) = \int_a^b e^{i\omega t} dX(\omega) - e^{ibt}\tilde{X}(b) + e^{iat}\tilde{X}(a), \tag{45}$$

$$\tilde{X}(\omega) = X(\omega) - \overline{X}(\omega). \tag{46}$$

From (42), (43) we see that

$$\underset{\substack{a \to -\infty \\ b \to \infty}}{\text{l.i.m.}}\ e^{ibt}\tilde{X}(b) - e^{iat}\tilde{X}(a) = 0 \tag{47}$$

Thus, applying the limit as $a \to -\infty$ and $b \to \infty$ to (45), (35) follows.

It is important to note that $\hat{X}(\omega)$ has orthogonal increments if, and only if, $X(\omega)$ is continuous in q.m. on the real line, as can be seen by

$$E([\hat{X}(\omega_4)-\hat{X}(\omega_3)][\hat{X}(\omega_2)-\hat{X}(\omega_1)]^*) = \begin{cases} 0 & , \ \omega_2 < \omega_3 \\ \frac{1}{2}[F(\omega_3+)-F(\omega_3-)], & \omega_2 = \omega_3 \end{cases} \tag{48}$$

whenever $\omega_1 < \omega_2 \le \omega_3 < \omega_4$. Thus, $\hat{X}(\omega)$ cannot be used in place of

$\overline{X}(\omega)$, although it has symmetry about its discontinuity points.

Lemma 4

Let $\{x(t),\ t\varepsilon R\}$ be a real, second order stationary process, continuous in q.m.. Let $\overline{X}(\omega)$ be given by (34). Then,

$$\left[\overline{X}(\omega_2)-\overline{X}(\omega_1)\right]^* = \overline{X}(-\omega_1)-\overline{X}(-\omega_2), \quad \omega_1,\ \omega_2 \neq 0 \tag{49}$$

$$\overline{X}^*(\omega) + \overline{X}(-\omega) = Z, \qquad \omega \neq 0 \tag{50}$$

where Z is a real random variable. Furthermore, ω is a continuity point if, and only if $-\omega$ is a continuity point.

Proof:

Using (7), we have

$$\left[\hat{X}(\omega_2)-\hat{X}(\omega_1)\right]^* = \underset{\tau \to \infty}{\text{l.i.m.}}\ \frac{1}{2\pi}\int_{-\tau}^{\tau} x(t)\ \frac{e^{i\omega_1 t}-e^{i\omega_2 t}}{-it}\ dt \tag{51}$$

$$= \underset{\tau \to \infty}{\text{l.i.m.}}\ \frac{1}{2\pi}\int_{-\tau}^{\tau} x(t)\ \frac{e^{i\omega_2 t}-e^{i\omega_1 t}}{it}\ dt \tag{52}$$

$$= \hat{X}(-\omega_1)-\hat{X}(-\omega_2), \quad \omega_1,\ \omega_2 \varepsilon R. \tag{53}$$

Since $\overline{X}(\omega)$ and $\hat{X}(\omega)$ are identical except on a countable set of discontinuity points, (49) holds except on the discontinuities. As $\overline{X}(\omega)$ is continuous from the left for $\omega \geq 0$, and from the right for $\omega < 0$, (49) holds by applying the appropriate limits. Rearranging (49),

$$\overline{X}^*(\omega_2) + \overline{X}(-\omega_2) = \overline{X}^*(\omega_1) + \overline{X}(-\omega_1) = Z, \quad \omega_1, \omega_2 \neq 0 \tag{54}$$

so that Z does not depend on the value ω. To see that Z must be real, it suffices to set $\omega_1 = -\omega_2$

$$Z = \overline{X}^*(\omega_2) + \overline{X}(-\omega_2) = \overline{X}^*(-\omega_2) + \overline{X}(\omega_2) = Z^*. \tag{55}$$

Now let $\omega_2 = \omega + h$, $\omega_1 = \omega$; then

$$E|\overline{X}(\omega+h) - \overline{X}(\omega)|^2 = E|\overline{X}(-\omega-h) - \overline{X}(-\omega)|^2, \quad \omega \neq 0, \ \omega+h \neq 0. \tag{56}$$

Hence, as $h \to 0$ $(\omega+h \neq 0)$, either both limits converge to zero and $\overline{X}(\omega)$ is continuous in q.m. at ω and $-\omega$, or (exclusive) $\overline{X}(\omega)$ is not continuous at either point. Thus, the assertion is proved.

Theorem 2

Let $\{x(t), t \varepsilon R\}$ be a real, Gaussian, second order stationary random process, continuous in q.m.. Then the two-sided sideband signals $\{x_k(t) + x_{-k}(t), \ t \varepsilon R\}$, $k = 0, 1, 2, \ldots$, are statistically independent, second order stationary, real Gaussian random processes, where

$$x_k(t) = \int_{-\omega_0/2}^{\omega_0/2} e^{i\omega t} d\overline{X}_k(\omega), \quad k = 0, \pm 1, \ldots, \quad \omega_0 > 0, \tag{57}$$

$$\overline{X}_k(\omega) = \overline{X}(\omega + k\omega_0) - \overline{X}(k\,\omega_0) \qquad \omega \varepsilon [-\omega_0/2, \ \omega_0/2). \tag{58}$$

The two-sided sidebands $\{\overline{X}_k(\omega) + \overline{X}_{-k}(\omega), \ \omega \varepsilon [-\omega_0/2, \ \omega_0/2)\}$, $k=0, 1, \ldots$, are statistically independent, Gaussian random processes with orthogonal increments.

Proof:

From Lemma 1, recall that the sideband signals are uncorrelated and second order stationary. Thus,

$$E([x_k(t)+x_{-k}(t)][x_j(t')+x_{-j}(t')]^*)=[R_k(t-t')+R_{-k}(t-t')]\delta_{k-j},\ k,j=0,1,\ldots, \tag{59}$$

So that the two-sided sideband signals are also uncorrelated and second order stationary. Hence, to obtain independence, it suffices to show that the processes are strongly Gaussian. First note that $\overline{X}(\omega)$ and, hence, $\overline{X}_k(\omega)$, $x_k(t)$ are Gaussian; e.g. see Loève, pp. 485-486.

$$x_k^*(t) = \left[\int_{-\omega_0/2}^{\omega_0/2} e^{i\omega t} d\overline{X}_k(\omega)\right]^* = \int_{-\omega_0/2}^{\omega_0/2} e^{-i\omega t} d\overline{X}_k^*(\omega) \tag{60}$$

$$= \int_{-\omega_0/2}^{\omega_0/2} e^{-i\omega t} d\overline{X}_{-k}(-\omega) = \int_{-\omega_0/2}^{\omega_0/2} e^{i\omega t} d\overline{X}_{-k}(\omega) = x_{-k}(t)\ , \tag{61}$$

where we have used Lemma 4, and the continuity of $e^{i\omega t}$. To see this in more detail, consider the partition $-\omega_0/2 = \omega_1 < \omega_2 < \ldots < \omega_{n+1} = \omega_0/2$. The Riemann-Stieltjes sums are

$$\left(\left(\sum_{j=1}^{n} e^{i\omega_j' t}\left[\overline{X}_k(\omega_{j+1}) - \overline{X}_k(\omega_j)\right]\right)\right)^* = \sum_{j=1}^{n} e^{-i\omega_j' t}\left[\overline{X}(\omega_{j+1}+k\omega_0)-\overline{X}(\omega_j+k\omega_0)\right]^* \tag{62}$$

$$= \sum_{j=1}^{n} e^{i(-\omega_j')t}\left[\overline{X}(-\omega_j-k\omega_0)-\overline{X}(-\omega_{j+1}-k\omega_0)\right] \tag{63}$$

$$= \sum_{j=1}^{n} e^{i(-\omega_j')t}\left[\overline{X}_{-k}(-\omega_j)-\overline{X}_{-k}(-\omega_{j+1})\right] \tag{64}$$

$$= \sum_{j=1}^{n} e^{i\overline{\omega}_j' t}\left[\overline{X}_{-k}(\overline{\omega}_{j+1})-\overline{X}(\overline{\omega}_j)\right] \tag{65}$$

where $\{\bar{\omega}_j,\ j = 1, 2, \ldots, n+1\}$ is the partition

$$-\omega_0/2 = \bar{\omega}_1 = -\omega_{n+1} < \bar{\omega}_2 = -\omega_n < \ldots < \bar{\omega}_{n+1} = -\omega = \omega_0/2 \tag{66}$$

$$\bar{\omega}'_j = -\omega'_{n+1-j},\ j = 1, 2, \ldots, n. \tag{67}$$

As the norm of the partition approaches zero, the sums on the LHS of (62) approach $x_k^*(t)$, while (65) approaches $x_{-k}(t)$. Thus, $x_k(t) + x_{-k}(t)$ is real, hence strongly Gaussian, and independence follows.

From Lemma 1, recall that the sidebands are uncorrelated and have orthogonal increments, hence the sum of any two and, in particular, the two-sided sidebands have orthogonal increments. Now, let

$$Y_k(\omega) = \bar{X}_k(\omega) + \bar{X}_{-k}(\omega), \quad -\omega_0/2 \leq \omega < \omega_0/2. \tag{68}$$

Then,

$$Y_k^*(\omega) = \bar{X}_k^*(\omega) + \bar{X}_{-k}^*(\omega) = -\bar{X}_{-k}(-\omega) - \bar{X}_k(-\omega) = -Y_k(-\omega) \tag{69}$$

$$E(Y_k(\omega)\, Y_j(\omega')) = -E(Y_k(\omega)\, Y_j^*(-\omega')) = 0,\ k \neq j \tag{70}$$

Thus, the two-sided sidebands $\{Y_k(\omega),\ \omega \varepsilon \left[-\omega_0/2,\ \omega_0/2\right)\}$ are strongly Gaussian and uncorrelated; it follows that they are independent, and the proof is complete.

It is of interest to note that $\{\bar{X}(\omega),\ \omega \varepsilon R\}$ does not have independent increments except for the trivial case where it is constant except for a possible jump at $\omega=0$, which corresponds to $x(t)$ having sample functions which are constant. This can be seen from

$$E\left(\left[\overline{X}(\omega_2)-\overline{X}(\omega_1)\right]\left[\overline{X}(-\omega_1)-\overline{X}(-\omega_2)\right]\right) = \overline{F}(\omega_2)-\overline{F}(\omega_1), \tag{71}$$

whenever $0 \leq \omega_1 < \omega_2$. The following lemma will be needed for Theorem 3.

Lemma 5

Let $\{X_n(\omega),\ a \leq \omega \leq b\}$ $n = 1, 2, \ldots$ be processes with jointly orthogonal increments such that

$$E|X_n(\omega_2) - X_n(\omega_1)|^2 = F_n(\omega_2) - F_n(\omega_1), \quad \omega_1 \leq \omega_2 \tag{72}$$

$$X(\omega) = \underset{n \to \infty}{\text{l.i.m.}}\ X_n(\omega), \quad a \leq \omega \leq b \tag{73}$$

Let f be a bounded complex function on $[a, b]$. If the integrals below exist, then

$$\int_a^b f(\omega)\ dX(\omega) = \underset{n \to \infty}{\text{l.i.m.}} \int_a^b f(\omega)\ dX_n(\omega), \tag{74}$$

and $\{X(\omega),\ a \leq \omega \leq b\}$ has orthogonal increments.

Proof:

$$\text{Let } \Delta_i X_n = X_n(\omega_i) - X_n(\omega_i'), \quad i = 1, 2. \tag{75}$$

Then, whenever $\omega_1' < \omega_1 \leq \omega_2' < \omega_2$,

$$E(\Delta_2 X\ \ \Delta_1 X^*) = \lim_{n\to\infty} E(\Delta_2 X_n\ \ \Delta_1 X_n^*) = 0. \tag{76}$$

Hence, $X(\omega)$ has orthogonal increments. Since $X_n(\omega)$, $X_m(\omega)$ have jointly orthogonal increments, i.e.,

$$E(\Delta_2 X_m \quad \Delta_1 X_n^*) = 0, \tag{77}$$

it follows that

$$E(\Delta_2 X \quad \Delta_1 X_n^*) = \lim_{m\to\infty} E(\Delta_2 X_m \quad \Delta_1 X_n^*) = 0. \tag{78}$$

Thus, by direct computation, it can be seen that the process

$$\tilde{X}_n(\omega) = X(\omega) - X_n(\omega) \xrightarrow{q.m.} 0, \; a \le \omega \le b, \tag{79}$$

also has orthogonal increments. Now,

$$E\left|\int_a^b f(\omega)\, dX(\omega) - \int_a^b f(\omega)\, dX_n(\omega)\right|^2 = E\left|\int_a^b f(\omega)\, d\tilde{X}_n(\omega)\right|^2 \tag{80}$$

$$= \int_a^b |f(\omega)|^2 \, d\tilde{F}_n(\omega) \tag{81}$$

$$\le \int_a^b M^2 \, d\tilde{F}_n(\omega) = M^2\left[\tilde{F}_n(b) - \tilde{F}_n(a)\right] \to 0, \tag{82}$$

where M is an upper bound on f, and

$$\tilde{F}_n(\omega_2) - \tilde{F}_n(\omega_1) = E\left|\tilde{X}_n(\omega_2) - \tilde{X}_n(\omega_1)\right|^2, \; \omega_1 \le \omega_2 \tag{83}$$

Hence, (74) follows.

<u>Theorem 3</u>

Let $\{x(t), t\epsilon R\}$ be second order stationary and continuous in q.m. Then,

$$x_r(t) = \underset{m,n\to\infty}{\text{l.i.m.}} \sum_{k=-m}^{n} x_k(t) = x_0(t) + x_a(t), \; t\epsilon R, \tag{84}$$

$$X_r(\omega) = \underset{m,n\to\infty}{\text{l.i.m.}} \sum_{k=-m}^{n} \overline{X}_k(\omega) = \overline{X}_0(\omega) + X_a(\omega), \quad \frac{-\omega_0}{2} \le \omega < \frac{\omega_0}{2}, \tag{85}$$

$$x_r(t) = \int_{-\omega_0/2}^{\omega_0/2} e^{i\omega t}\, dX_r(\omega), \quad t\varepsilon R, \tag{86}$$

$$E|X_r(\omega_2) - X_r(\omega_1)|^2 = \sum_{k=-\infty}^{\infty} \overline{F}(\omega_2+k\omega_0) - \overline{F}(\omega_1+k\omega_0) = F_r(\omega_2) - F_r(\omega_1), \omega_1 \le \omega_2 \tag{87}$$

$$E(x_r(t)\, x_r^*(t')) = \int_{-\omega_0/2}^{\omega_0/2} e^{i\omega(t-t')} dF_r(\omega). \tag{88}$$

$x_0(t)$ $(\overline{X}_0(\omega))$ and $x_a(t)$ $(X_a(\omega))$ are uncorrelated. Furthermore, if $x(t)$ is real and Gaussian, then $x_0(t)$ and $x_a(t)$ are statistically independent, real, Gaussian processes; $\overline{X}_0(\omega)$ and $X_a(\omega)$ are statistically independent, Gaussian processes. The processes $x_a(t)$ $(X_a(\omega))$ will be called the aliasing error signal (aliasing error IFT).

Proof:

To show the convergence in (84), recall that (Lemma 1), the sideband signals are uncorrelated. Using (25), we obtain

$$E\left|\sum_{k=-m}^{n} x_k(t)\right|^2 = \sum_{k=-m}^{n} E|x_k(t)|^2 = \sum_{k=-m}^{n} \overline{F}_k\left(\frac{\omega_0}{2}\right) - \overline{F}_k\left(-\frac{\omega_0}{2}\right) \tag{89}$$

$$= \sum_{k=-m}^{n} \overline{F}\left(\frac{\omega_0}{2} + k\omega_0\right) - \overline{F}\left(-\frac{\omega_0}{2} + k\omega_0\right)$$

$$= \overline{F}\left(\frac{\omega_0}{2} + n\omega_0\right) - \overline{F}\left(-\frac{\omega_0}{2} - m\omega_0\right) \le \overline{F}(\infty) - \overline{F}(-\infty) < \infty, \tag{90}$$

which is sufficient for the desired convergence (e.g., Loève [21], p. 456). Similarly, for $\omega\varepsilon[-\omega_0/2, \omega_0/2)$,

$$E\left|\sum_{k=-m}^{n} \overline{X}_k(\omega)\right|^2 = E\left|\sum_{k=-m}^{n} \overline{X}(\omega+k\omega_0) - \overline{X}(k\omega_0)\right|^2 \tag{91}$$

$$= \sum_{k=-m}^{n} E\left|\overline{X}(\omega+k\omega_0) - \overline{X}(k\omega_0)\right|^2 \tag{92}$$

$$= \sum_{k=-m}^{n} \left|\overline{F}(\omega+k\omega_0) - \overline{F}(k\omega_0)\right| \tag{93}$$

$$\leq \sum_{k=-m}^{n} \overline{F}\left(\frac{\omega_0}{2} + k\omega_0\right) - \overline{F}\left(-\frac{\omega_0}{2} + k\omega_0\right) \leq \overline{F}(\infty) - \overline{F}(-\infty). \tag{94}$$

Thus, the limit in (85) exists, and $X_r(\omega)$ is defined.

$$E\left|X_r(\omega_2) - X_r(\omega_1)\right|^2 = E\left|\sum_{k=-\infty}^{\infty} \overline{X}_k(\omega_2) - \overline{X}_k(\omega_1)\right|^2 \tag{95}$$

$$= \sum_{k=-\infty}^{\infty} E\left|\overline{X}_k(\omega_2) - \overline{X}_k(\omega_1)\right|^2 \tag{96}$$

$$= \sum_{k=-\infty}^{\infty} \overline{F}(\omega_2+k\omega_0) - \overline{F}(\omega_1+k\omega_0) \tag{97}$$

results in (87), where Lemma 1 has been used. Now, to show (86), let

$$X_{rn}(\omega) = \sum_{k=-n}^{n} \overline{X}_k(\omega) \xrightarrow{q.m.} X_r(\omega), \tag{98}$$

$$x_{rn}(t) = \sum_{k=-n}^{n} x_k(t) \xrightarrow{q.m.} x_r(t). \tag{99}$$

$$x_{rn}(t) = \sum_{k=-n}^{n} \int_{-\omega_0/2}^{\omega_0/2} e^{i\omega t} d\overline{X}_k(\omega) = \int_{-\omega_0/2}^{\omega_0/2} e^{i\omega t} dX_{rn}(\omega). \tag{100}$$

Using (16) in Lemma 1, note that

$$E(\Delta_2 X_{rn} \quad \Delta_1 X^*_{rm}) = E(\sum_{k=-n}^{n} \Delta_2 \overline{X}_k \sum_{j=-m}^{m} \Delta_1 X^*_j) \tag{101}$$

$$= \sum_{k=-n}^{n} \sum_{j=-m}^{m} E(\Delta_2 \overline{X}_k \quad \Delta_1 \overline{X}^*_j) \tag{102}$$

$$= \sum_{k=-p}^{p} E(\Delta_2 \overline{X}_k \quad \Delta_1 \overline{X}^*_k) = 0, \tag{103}$$

whenever the increments $\Delta_i X_k$ (defined by 75) correspond to disjoint intervals, and $p = \min(n, m)$. Hence the processes, $X_{rn}(\omega)$, have jointly orthogonal increments, and Lemma 5 applies. Taking the limit as $n \to \infty$ of both sides of (100) results in (86). By Lemma 5, $\{X_r(\omega), \ -\frac{\omega_0}{2} \le \omega < \frac{\omega_0}{2}\}$ has orthogonal increments; thus,

$$E(x_r(t)\, x^*_r(t')) = E(\left[\int_{-\omega_0/2}^{\omega_0/2} e^{i\omega t} dX_r(\omega)\right]\left[\int_{-\omega_0/2}^{\omega_0/2} e^{i\omega t'} dX_r(\omega)\right]^*) \tag{104}$$

$$= \int_{-\omega_0/2}^{\omega_0/2} e^{i\omega(t-t')} dF_r(\omega). \tag{105}$$

If $x(t)$ is real and Gaussian, to show the desired properties it suffices to note that $x_0(t)$, $x_a(t)$, $\overline{X}_0(\omega)$ and $X_a(\omega)$ can all be expressed in terms of the appropriate two-sided processes and apply Theorem 2.

$$x_0(t) = \tfrac{1}{2}\left[x_0(t) + x_{-0}(t)\right], \quad \overline{X}_0(\omega) = \tfrac{1}{2}\left[\overline{X}_0(\omega) + \overline{X}_{-0}(\omega)\right]. \tag{106}$$

$$x_a(t) = \sum_{k=1}^{\infty} \left[x_k(t) + x_{-k}(t)\right], \quad X_a(\omega) = \sum_{k=1}^{\infty} \left[\overline{X}_k(\omega) + \overline{X}_{-k}(\omega)\right]. \tag{107}$$

Since $x_0(t)$ $(\overline{X}_0(\omega))$ and $x_a(t)$ $(X_a(\omega))$ are Borel functions of independent processes, they are themselves independent, and the proof is

complete.

Corollary 1

Let $\{x(t),\ t\varepsilon R\}$ be second order stationary and continuous in q.m. If the IPS $F(\omega)$ is absolutely continuous on R, with PSD $S(\omega)$, then the PSD of the process $x_r(t)$, say $S_r(\omega)$, is given by

$$S_r(\omega) = \sum_{k=-\infty}^{\infty} S(\omega+k\omega_0),\ -\omega_0/2 \le \omega < \omega_0/2, \tag{108}$$

Proof:

From (87) we have

$$F_r(\omega_2) - F_r(\omega_1) = \lim_{n\to\infty} \sum_{k=-n}^{n} \int_{\omega_1}^{\omega_2} S(\omega+k\omega_0)\ d\omega \tag{109}$$

$$= \lim_{n\to\infty} \int_{\omega_1}^{\omega_2} \left[\sum_{k=-n}^{n} S(\omega+k\omega_0)\right] d\omega \tag{110}$$

Since $F(\omega)$ is non-decreasing, the PSD $S(\omega) \ge 0$, $\omega\varepsilon R$. Hence, the integrand in (110) is non-decreasing as $n \uparrow \infty$. By the Monotone Convergence Theorem,

$$F_r(\omega_2) - F_r(\omega_1) = \int_{\omega_1}^{\omega_2} \left[\sum_{k=-\infty}^{\infty} S(\omega+k\omega_0)\right] d\omega; \tag{111}$$

so that $F_r(\omega)$ is absolutely continuous and its derivative is given by (108).

REFERENCES

1. F. E. Nicodemus, Self Study Manual on Optical Radiation Measurements, National Bureau of Standards, Tech. Note 910-4 (1979).
2. P. Mertz and F. Grey, Theory of Scanning and Its Relation to Characteristics of Transmitted Signal in Telephotography and Television, Bell Sy. Tech. J. 13, 464 (1934).
3. O. H. Schade, Sr., Image Gradation, Graininess and Sharpness in Television and Motion Picture Systems, J. Soc. Motion Pict. Telev. Eng. 56, 131 (1951); 58, 181 (1952); 61, 97 (1953); 64, 593 (1955).
4. L. G. Callahan and W. M. Brown, One and Two-Dimensional Processing in Line Scanning Systems, Appl. Opt. 2, 401 (1963).
5. A. Macovski, Spatial and Temporal Analysis of Scanned Systems, Appl. Opt. 9, 1906 (1970).
6. L. M. Biberman, ed., Perception of Displayed Information (Plenum Press, 1973).
7. S. J. Katzberg, et al., Photosensor Aperture Shaping to Reduce Aliasing in Optical-Mechanical Line-Scan Imaging Systems, Appl. Opt. 12, 1054 (1973).
8. A. H. Robinson, Multidimensional Fourier Transforms and Image Processing with Finite Scanning Apertures, Appl. Opt. 12, 2344 (1973).
9. D. E. Pearson, Transmission and Display of Pictorial Information (John Wiley and Sons, 1975).
10. R. A. Gonsalves and P. S. Considine, Spot Shaping and Incoherent

Optical Smoothing for Raster Scanned Imagery, Opt. Eng. 15, 64 (1976).

11. W. K. Pratt, Digital Image Processing (John Wiley and Sons, 1978).

12. R. M. Bracewell, The Fourier Transform and Its Application (McGraw-Hill, 1965).

13. J. W. Goodman, Introduction to Fourier Optics (McGraw-Hill, 1968).

14. R. B. Blackman and J. W. Tukey, Measurement fo Power Spectra (Dover, 1968).

15. S. Tutumi, Spatial Filter Used in Scanning Optical Detection System, J. Elec. and Com. in Japan, 49 (1966).

16. T. Takagi and S. Tutumi, Statistical Properties of Radiance Spatial Distribution of Sky and Forrest Backgrounds, J. Elec. and Com. in Japan, 51-C (1968).

17. Y. Itakura, et al., Statistical Properties of the Background Noise for the Atmospheric Windows in the Intermediate Infrared Region, Infrared Physics 14 (Pergamon Press, 1974).

18. C. E. Shannon and W. Weaver, The Mathematical Theory of Communication, (The University of Illinois Press, 1964).

19. P. B. Fellgett and E. H. Linfoot, On the Assessment of Optical Images, Phil. Trans. R. Soc. 247, 269 (1955).

20. F. O. Huck and S. K. Park, Optical-Mechanical Line-scan Imaging Process: its Information Capacity and Efficiency, Appl. Opt. 14, 2508 (1975).

21. M. Loève, Probability Theory (D. Van Nostrand Co. Inc., 1963).

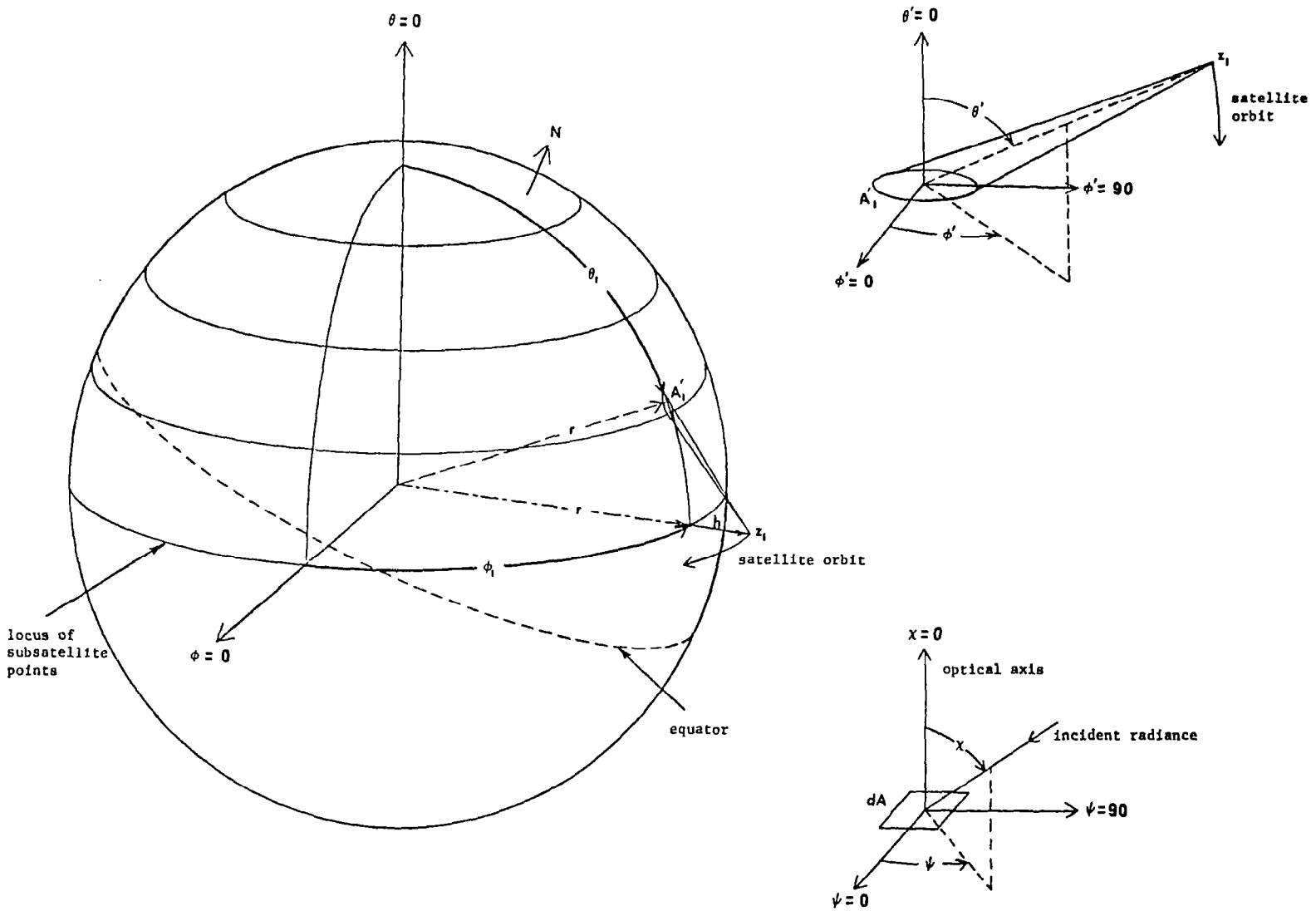

Figure 1 Satellite, Orbit and Top of the Atmosphere Geometry

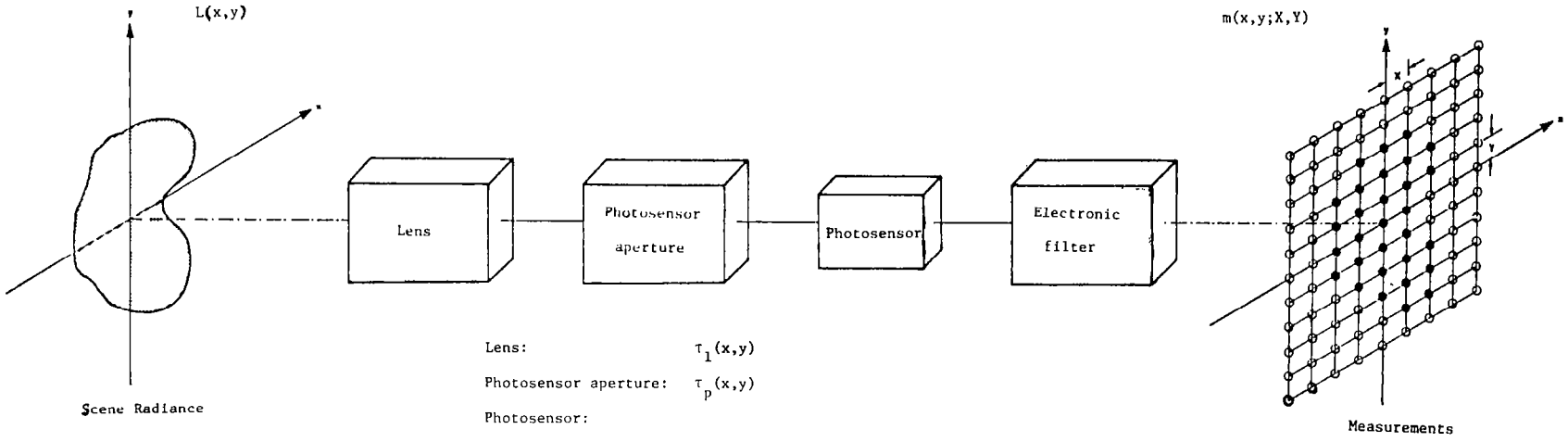

Lens: $\tau_l(x,y)$

Photosensor aperture: $\tau_p(x,y)$

Photosensor:

Electronic filter: $\delta(x)\tau_e(y)$

Radiometer response: $\tau(x,y) = \tau_e(x,y) * \tau_p(x,y) * \left[\delta(x)\tau_e(y)\right]$

Continuous signal: $m(x,y) = L(x,y) * \tau(x,y)$

Discrete measurements: $m(x,y;X,Y) = m(x,y)XY \sum_m \sum_n \delta(x-Xm,\ y-Yn)$

Figure 2 Block Diagram of NFOV Scanner

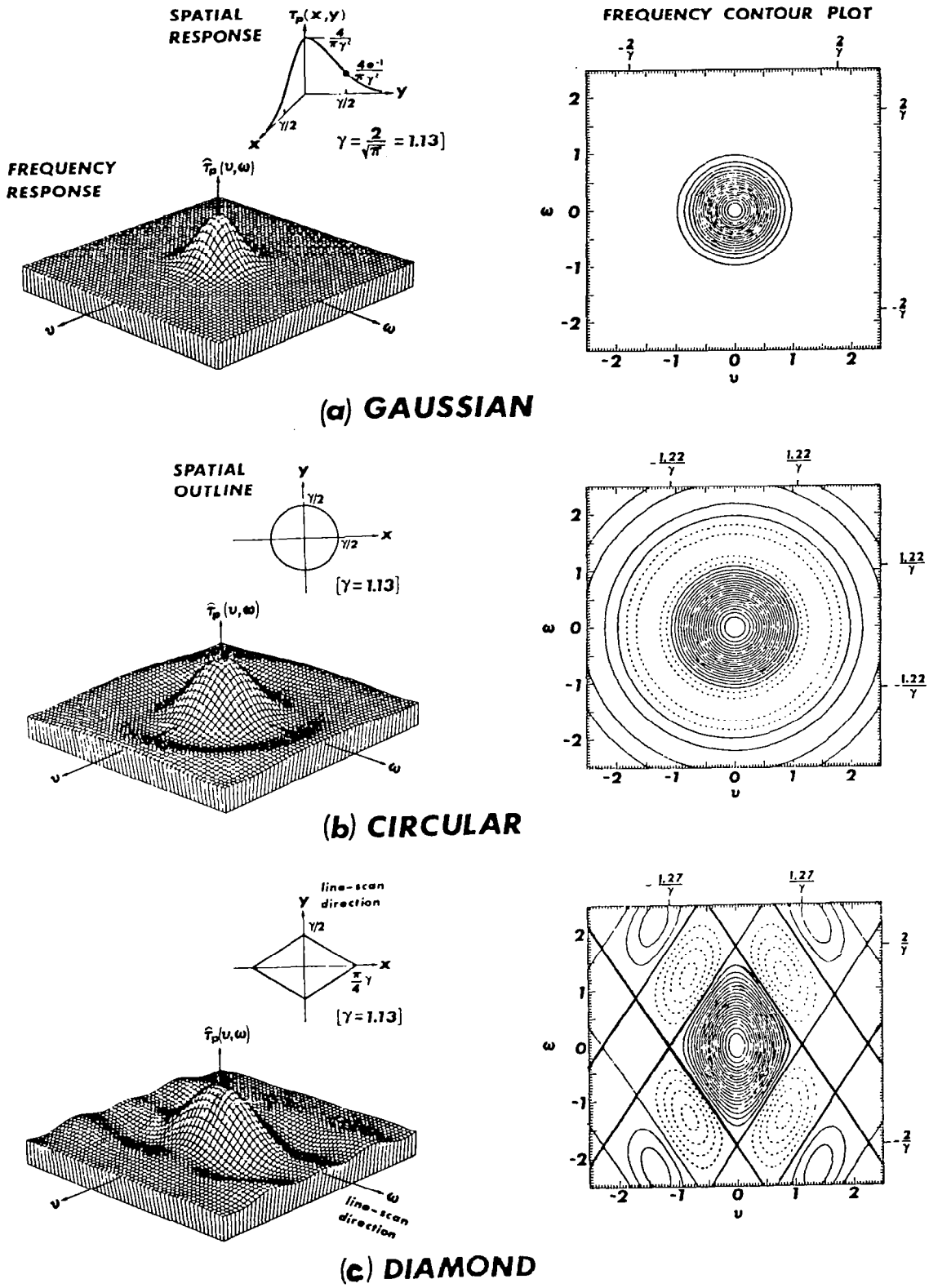

Figure 3 Frequency Response of Detectors

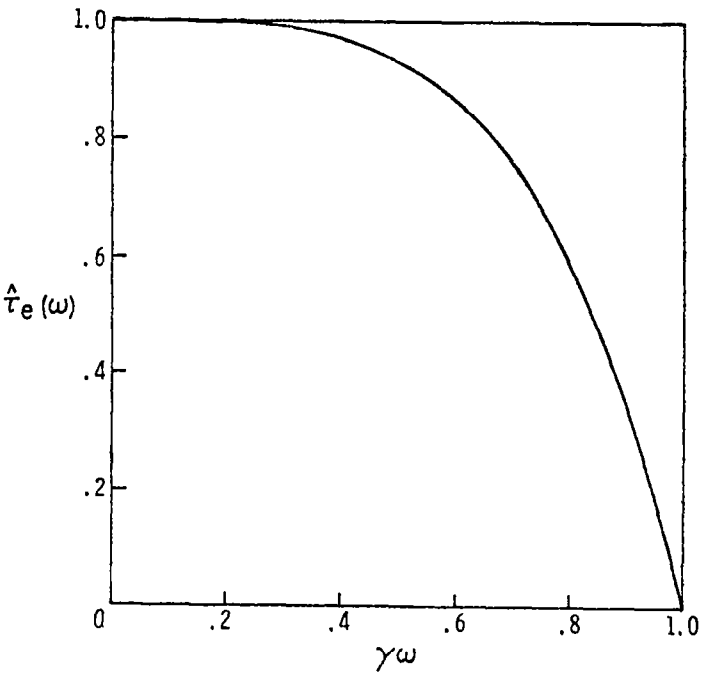

Figure 4 Frequency Response of Electrical Filters

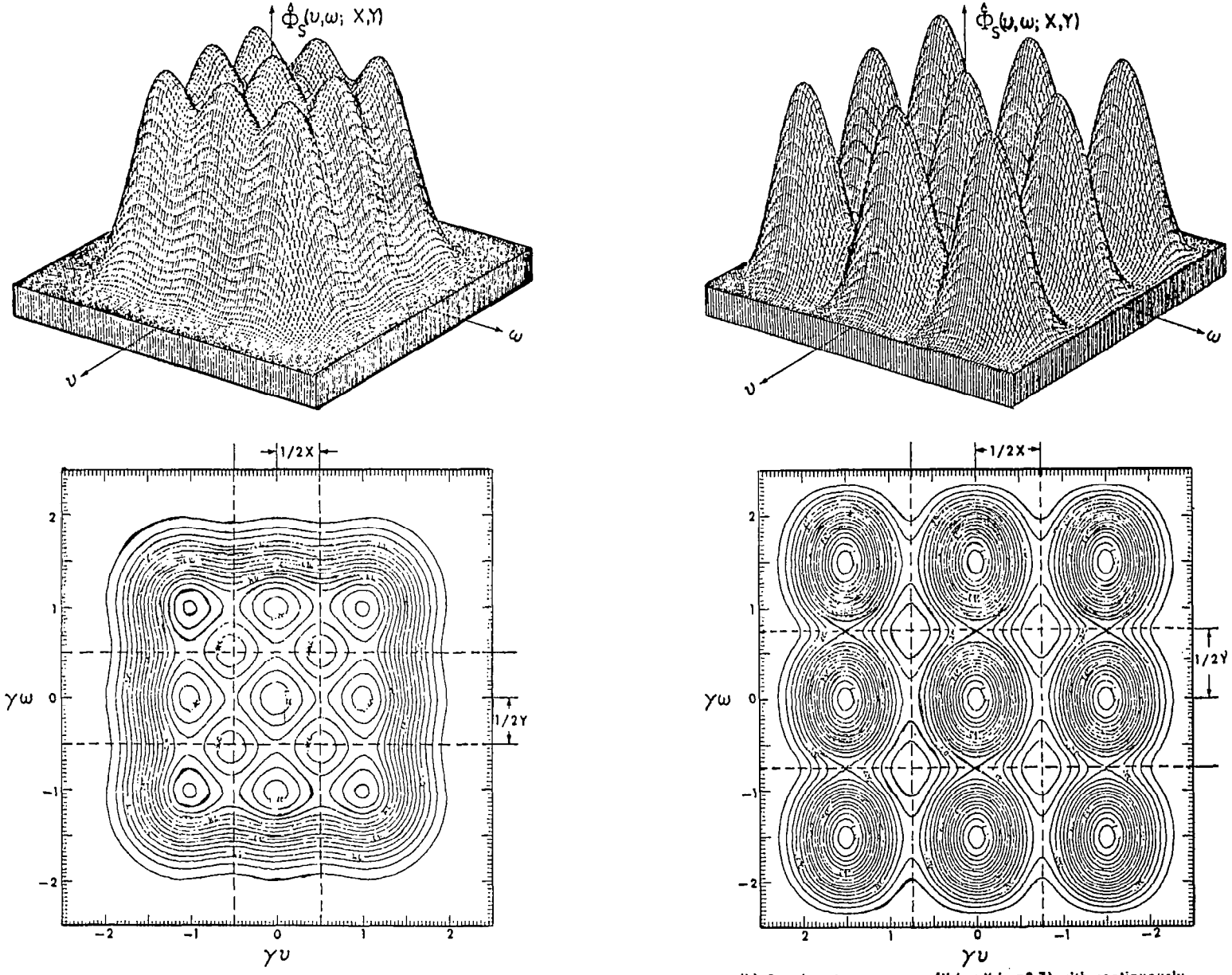

(a) Contiguous coverage (i.e., $X/\gamma = Y/\gamma = 1$) with discretely stepped circular photosensor aperture.

(b) Overlapping coverage ($X/\gamma = Y/\gamma = 0.7$) with continuously scanned diamond photosensor aperture and electronic filter.

Figure 5 Wiener Spectra of Sampled Signals

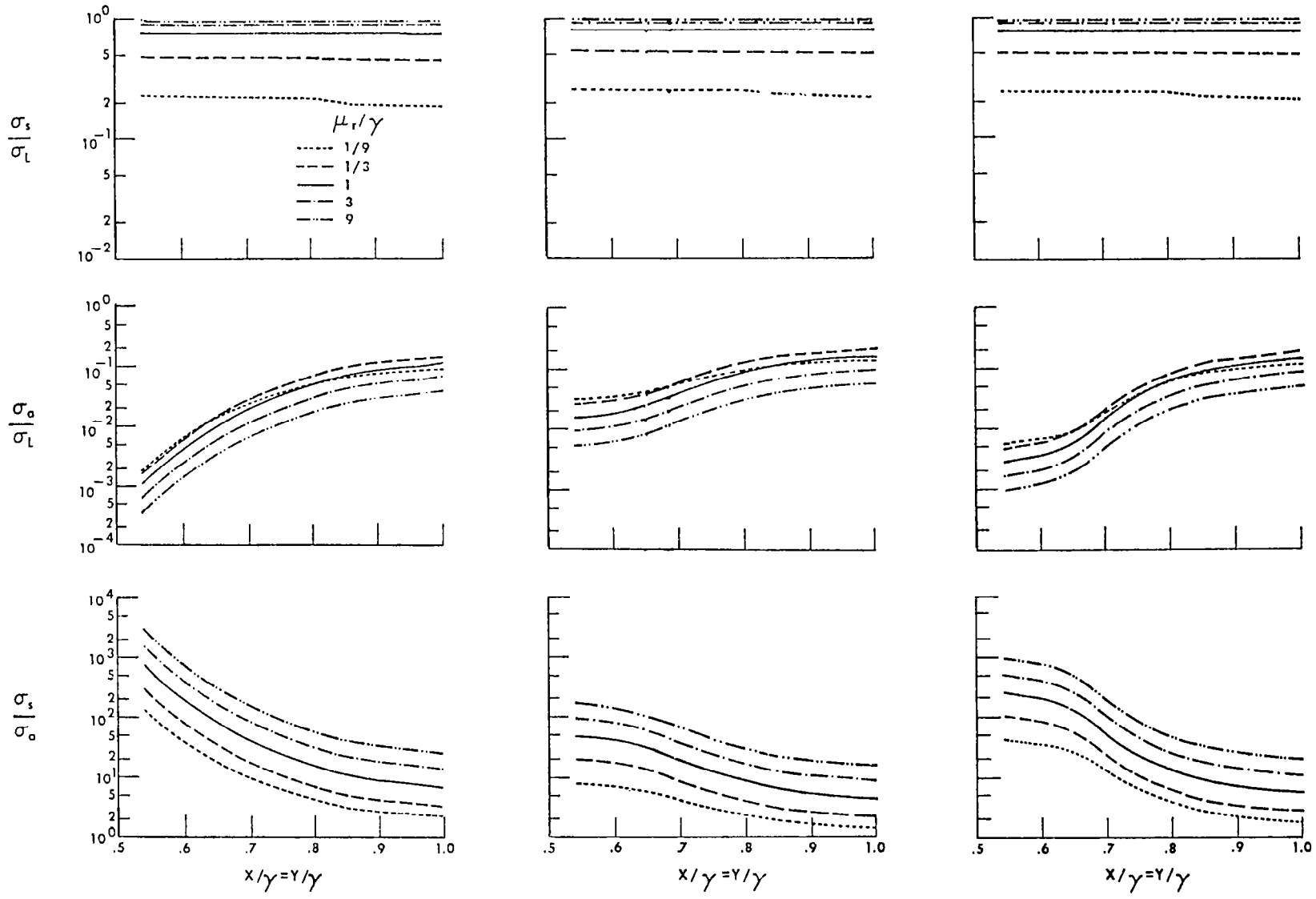

(a) Gaussian spot intensity profile (without electronic filter).

(b) Circular photosensor aperture shape (without electronic filter).

(c) Diamond photosensor aperture shape (with electronic filter).

Figure 6 Parametric Aliasing Error Curves.

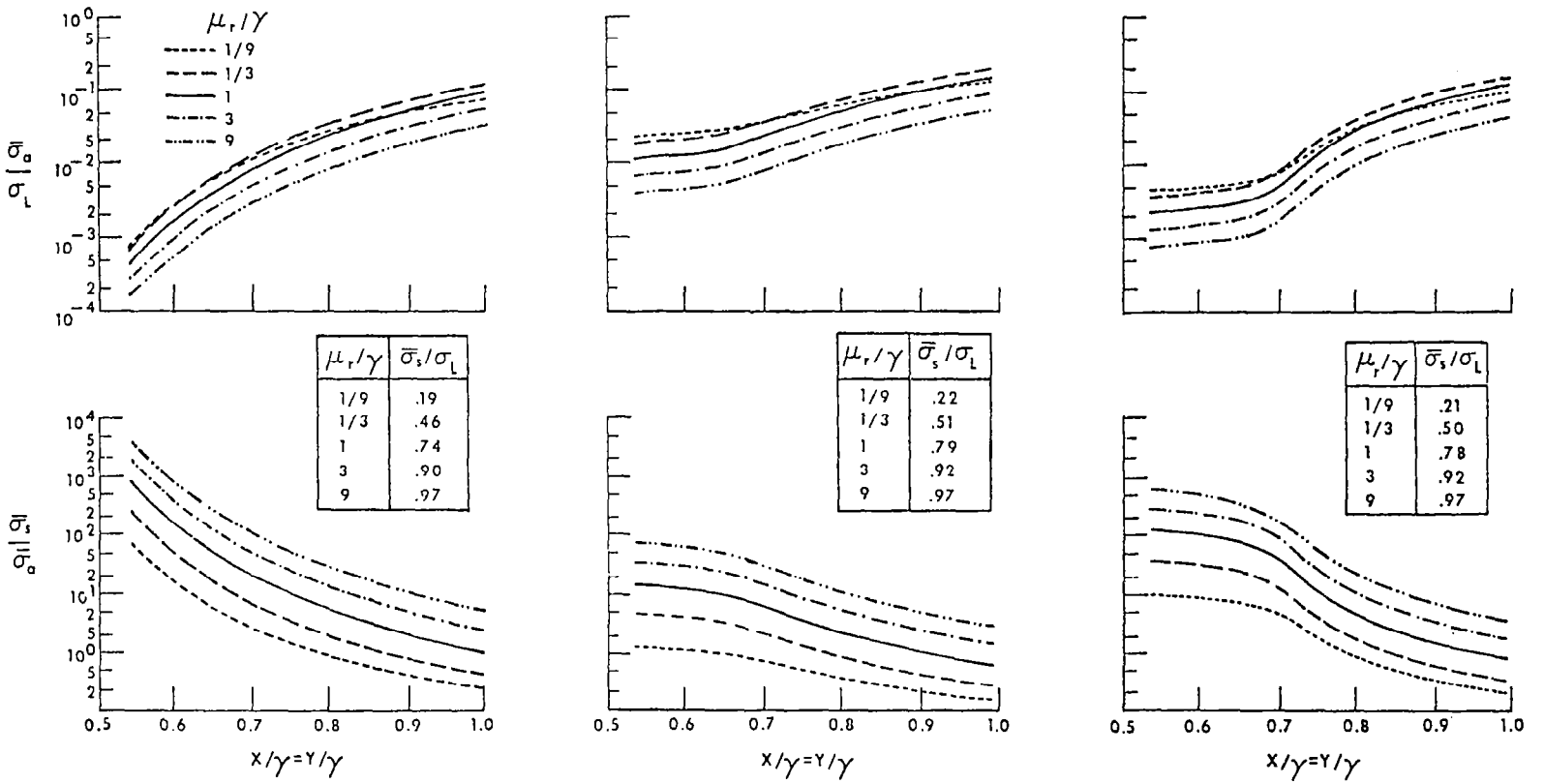

(a) Gaussian spot intensity profile (without electronic filter).

(b) Circular photosensor aperture shape (without electronic filter).

(c) Diamond photosensor aperture shape (with electronic filter).

Figure 7 Parametric Aliasing Error Curves of Smoothed Signals.

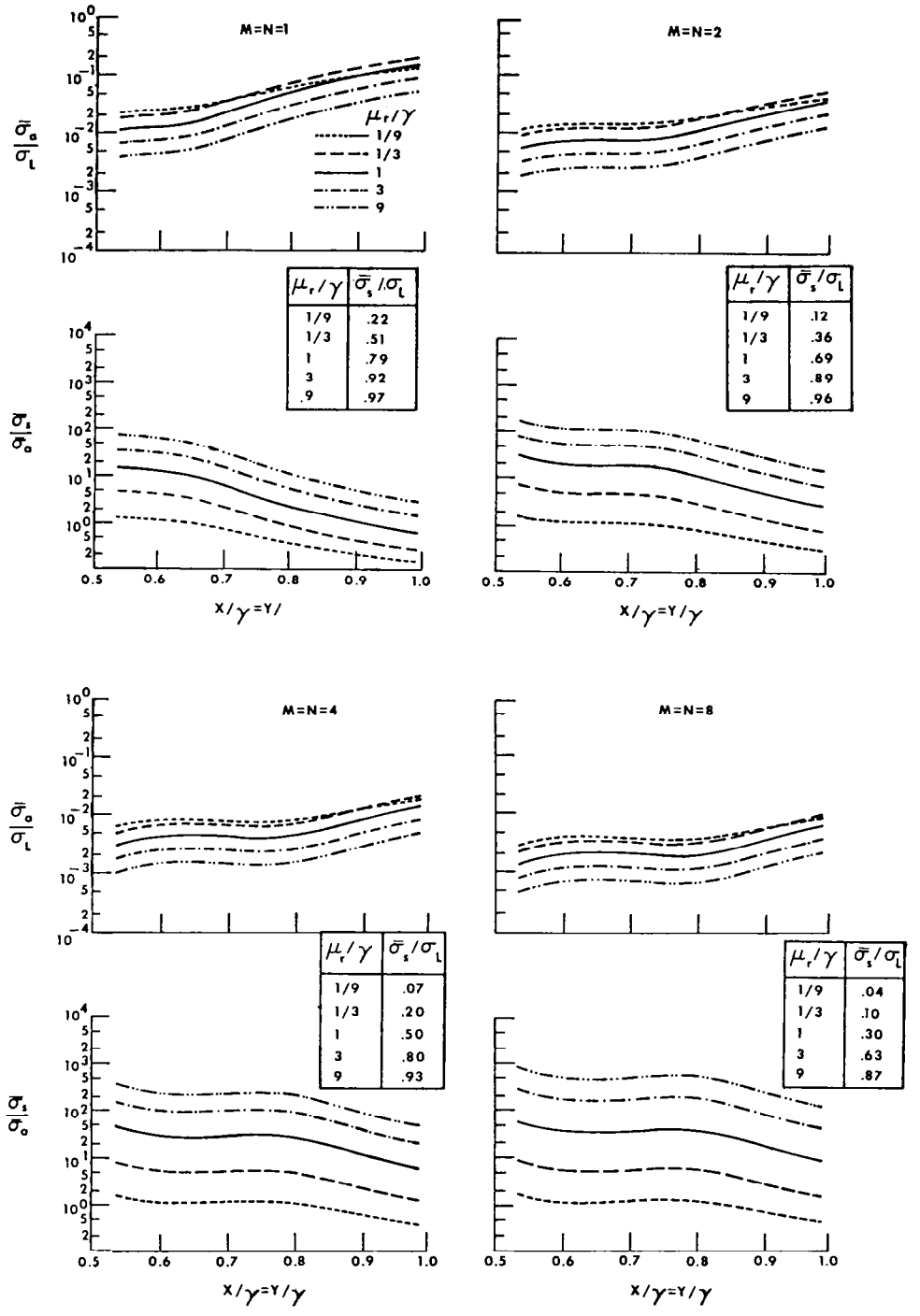

(d) Circular IFOV (without electronic filter).

Figure 7 Continued.

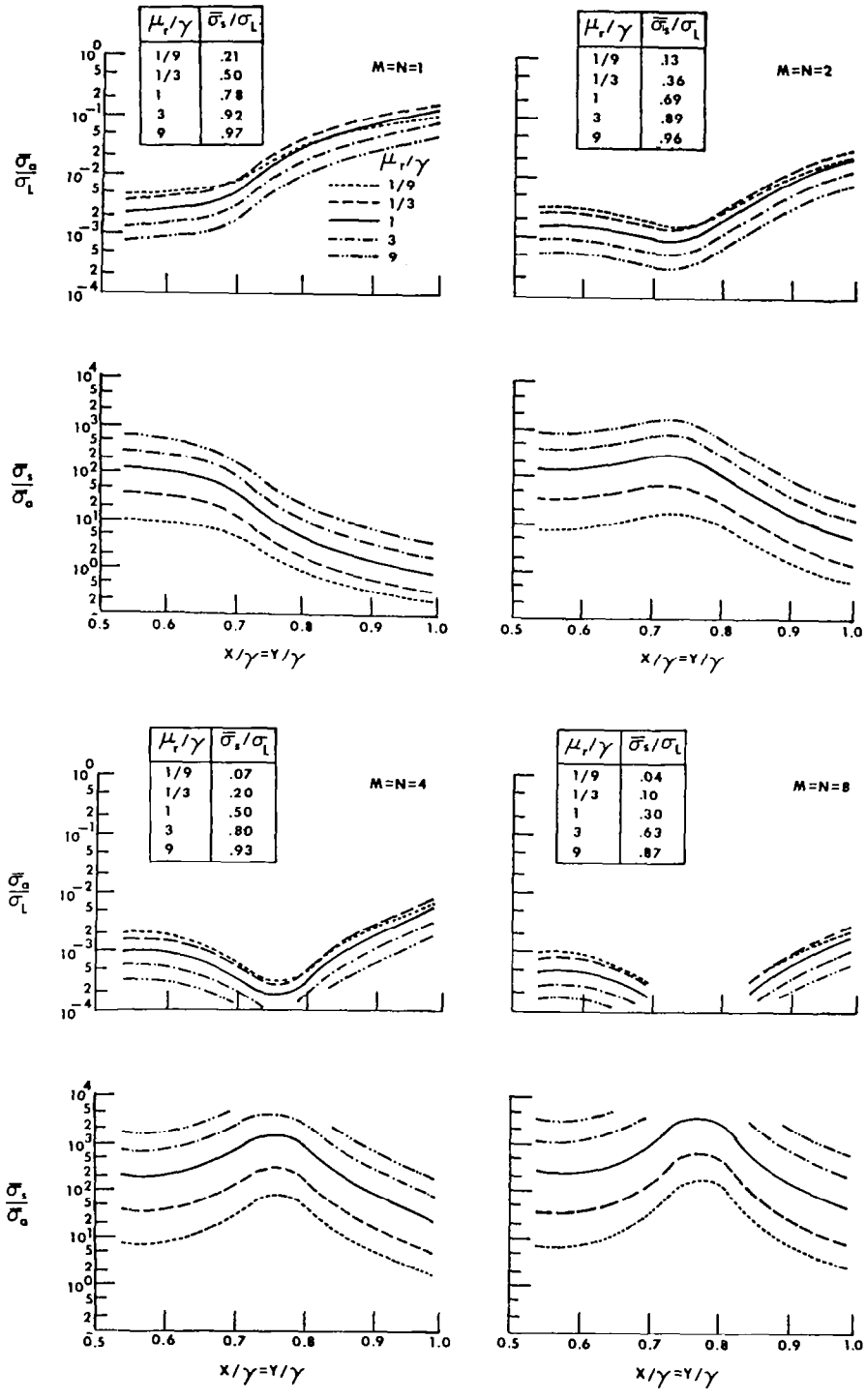

(e) Diamond IFOV (with electronic filter).

Figure 7 Concluded.

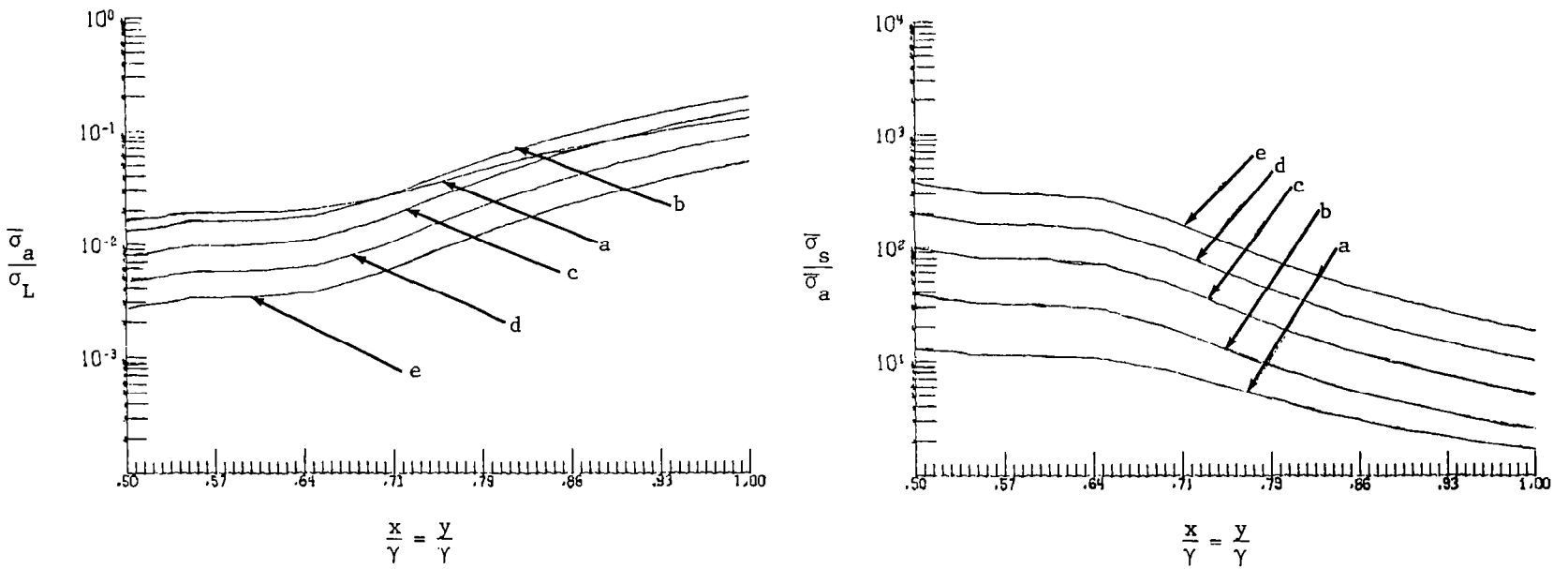

μ_r/γ: $a = \frac{1}{9}$; $a = \frac{1}{3}$; $c = 1$; $d = 3$; $e = 9$

Figure 8 Circular Aperture with Continuous Scan.

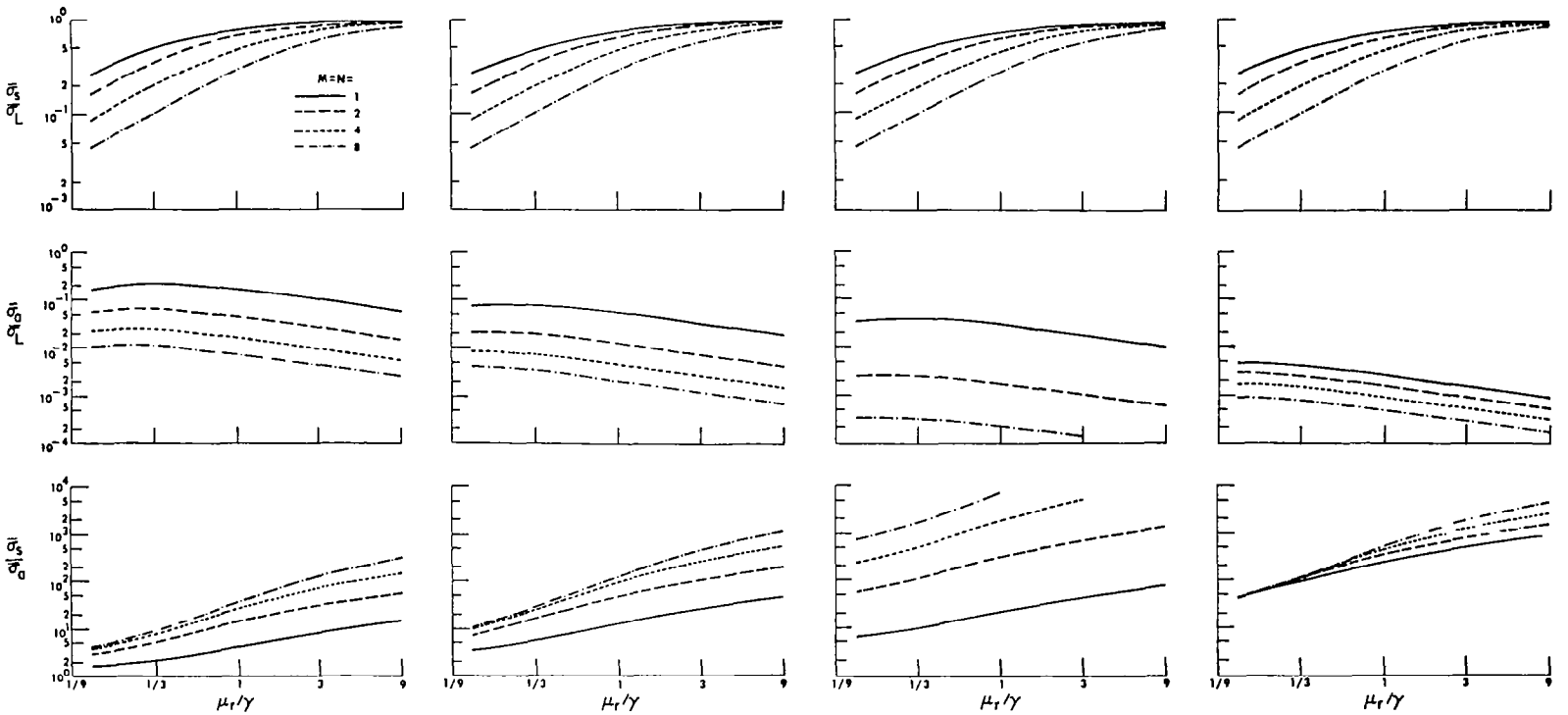

(a) Contiguous coverage ($X/\gamma = Y/\gamma = 1$) with discretely stepped, circular IFOV.

(b) Overlapping coverage ($X/\gamma = Y/\gamma = 0.6$) with discretely stepped, circular IFOV.

(c) Overlapping coverage ($X/\gamma = Y/\gamma = 0.8$) with continuously scanned diamond IFOV and electronic filter.

(d) Overlapping coverage ($X/\gamma = Y/\gamma = 0.6$) with continuously scanned diamond IFOV and electronic filter.

Figure 9 Aliasing Error Versus μ_r/γ for Smoothed Signals.

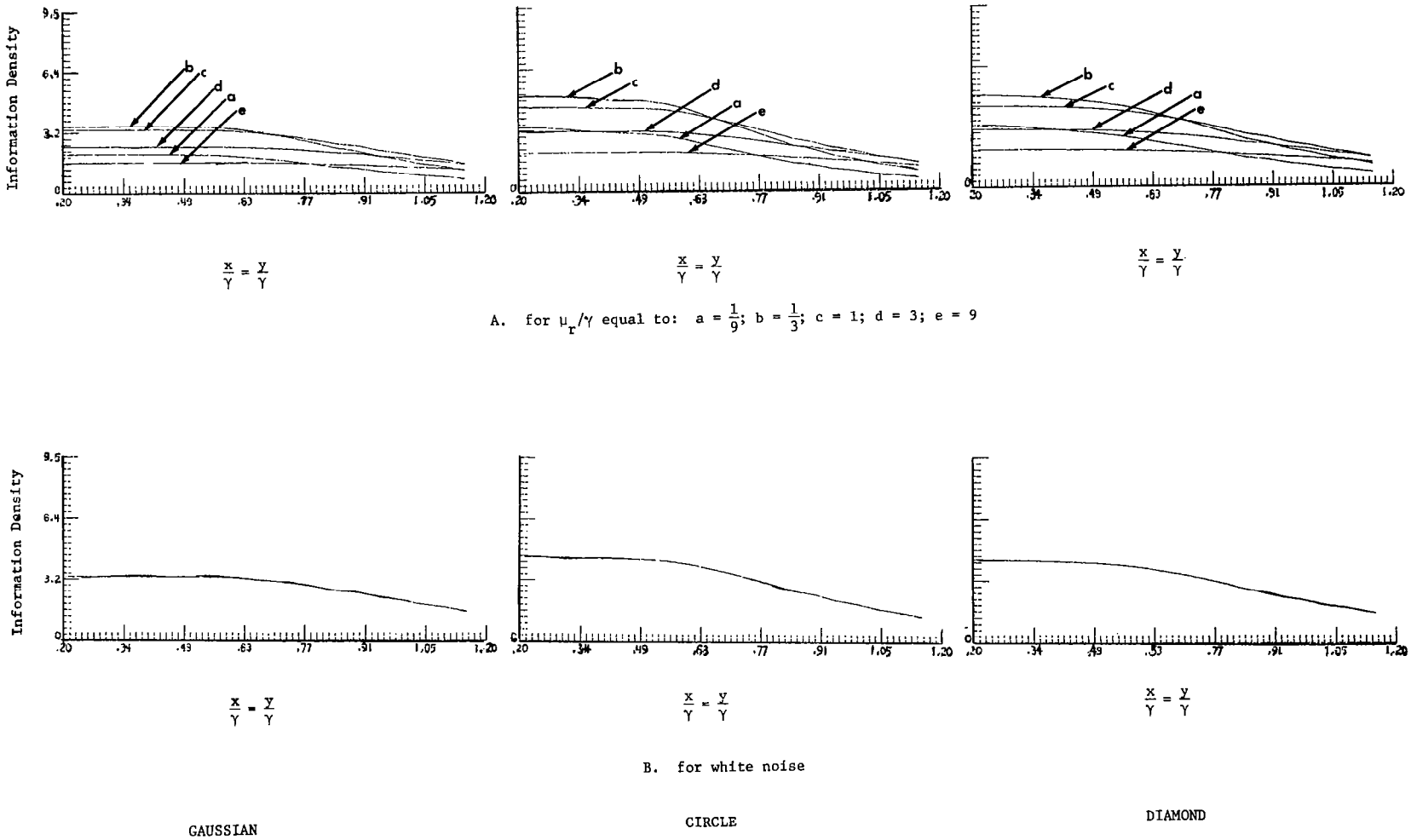

Figure 10 Information density transmitted through radiometer in unsmoothed reconstruction.

1. Report No.	2. Government Accession No.	3. Recipient's Catalog No.
NASA CR-3294		

4. Title and Subtitle	5. Report Date
A PARAMETRIC STUDY OF ALIASING ERROR FOR A NARROW FIELD OF VIEW SCANNING RADIOMETER	August 1980
	6. Performing Organization Code
7. Author(s)	8. Performing Organization Report No.
Nesim Halyo and Steven T. Stallman	FR-47801
	10. Work Unit No.
9. Performing Organization Name and Address	
Information & Control Systems, Incorporated 28 Research Drive Hampton, VA 23666	11. Contract or Grant No. NAS1-15628
	13. Type of Report and Period Covered
12. Sponsoring Agency Name and Address	Contractor Report
National Aeronautics and Space Administration Washington, DC 20546	14. Sponsoring Agency Code

15. Supplementary Notes

Langley Technical Monitor: Friedrich O. Huck
Final Report

16. Abstract

Starting from the general measurement equation, it is shown that a NFOV scanner can be approximated by a spatially invariant system whose point spread function depends on the detector shape and angular characteristics and electrical filter transfer function for given "patches" at the top of the atmosphere. The radiometer is modeled by a detector, electrical filter, A/D converter followed by a reconstruction filter. The errors introduced by aliasing and blurring into a reconstruction of the input radiant exitance are modeled and analyzed for various detector shapes, sampling intervals, electrical filters and scan types. Quantitative results on the errors introduced are presented showing the various trade-offs between design parameters. The results indicate that proper selection of detector shape coupled with electrical filter can reduce aliasing errors significantly.

17. Key Words (Suggested by Author(s))	18. Distribution Statement
radiometer, scanner detector shape, aliasing, blurring, information density, modeling	Unclassified-Unlimited Subject Category 35

19. Security Classif. (of this report)	20. Security Classif. (of this page)	21. No. of Pages	22. Price
Unclassified	Unclassified	78	A05

For sale by the National Technical Information Service, Springfield, Virginia 22161

NASA-Langley, 1980